

**PERFORMANCE EVALUATION OF NEW IMAGING  
TECHNOLOGIES FOR IN VIVO ASSESSMENT OF BONE HEALTH**

by  
Gengxin Shi

A thesis submitted to Johns Hopkins University in conformity with the  
requirements for the degree of Master of Science and Engineering

Baltimore, Maryland  
October 2020

# ABSTRACT

Research has shown that quantitative assessment of bone microstructure can be beneficial for early detection of musculoskeletal conditions such as osteoarthritis and osteoporosis. However, bone microstructure cannot be accurately measured using current generation x-ray systems due to their limited spatial resolution. Therefore, the present clinical practice relies primarily on the image-based metric of Bone Mineral Density (BMD), which does not distinguish different arrangements of trabecular microarchitecture.

We investigate whether the recently introduced computed tomography (CT) scanners with enhanced spatial resolution, specifically Complementary metal–oxide–semiconductor (CMOS) detector-based extremity Cone Beam CT (CBCT) and ultra-high resolution multi-detector CT (UHR-MDCT, e.g. Canon Aquilion Precision CT), could potentially enable quantitative assessment of trabecular microstructure in clinical settings. This could benefit the research, early detection, and monitoring of musculoskeletal conditions.

The performance of the new imaging systems is evaluated for applications in conventional Trabecular Morphometrics (including metrics of trabecular thickness, spacing, and number), in classification of trabeculae into Rods and Plates, and in texture analysis. Human cadaveric bone samples are used for the assessment. The biomarker results from the new imaging systems are compared to the gold-standard micro-CT. We also assess the accuracy and reproducibility of BMD measurements on extremity CMOS-CBCT using data from a pilot human subject study.

The study shows that CMOS-CBCT and UHR-MDCT are able to achieve improved bone microstructure measurements compared to conventional technologies. In terms of established biomarkers such as BMD and texture features, the new imaging systems provide a good degree of reproducibility, supporting the use of CMOS-CBCT and UHR-MDCT for those biomarkers in the same manner as currently done with conventional modalities. Our results offer motivation for future clinical translation of *in vivo* quantitative bone microstructure evaluation using the new high resolution CT technologies.

**Primary Reader and Advisor:** Wojciech Zbijewski  
**Secondary Reader:** Alejandro Sisniega and Ali Uneri

# **ACKNOWLEDGEMENT**

I would like to express my deepest gratitude to Professor Wojciech Zbijewski for introducing me to medical imaging research, and for his continuous guidance and support through my master's study.

# TABLE OF CONTENTS

|  |             |
|--|-------------|
| <b>Abstract</b>  | <b>ii</b>   |
| <b>Acknowledgements</b>  | <b>iv</b>   |
| <b>List of tables</b>  | <b>vii</b>  |
| <b>List of figures</b>   | <b>viii</b> |
| <b>Chapter 1</b>   | <b>1</b>    |
| Introduction .....   | 1           |
| 1.1.1 Significance .....   | 1           |
| 1.1.2 Osteoarthritis .....   | 2           |
| 1.1.3 Osteoporosis .....   | 3           |
| 1.2 Quantitative Assessment of Bone using X-ray Imaging.....                           | 4           |
| 1.2.1 Bone Mineral Density (BMD) .....   | 4           |
| 1.2.2 Radiomic Texture Analysis .....  | 5           |
| 1.2.3 Measurements of Trabecular Morphometry .....                                     | 6           |
| 1.2.4 Individual Trabecular Segmentation (ITS) to Assess Rod and Plate Morphology..... | 6           |
| 1.3 Emerging Modalities for Bone Imaging .....   | 7           |
| 1.3.1 Ultra-High Resolution MDCT (UHR-MDCT) .....                                      | 8           |
| 1.3.2 Extremity Cone Beam CT(CBCT) .....   | 8           |
| 1.3.3 Pixelated Columnar CsI:TI Scintillators.....                                     | 9           |
| 1.3.4 Performance Assessment .....   | 10          |
| 1.3.4.1 Trabecular Morphometry.....  | 10          |
| 1.3.4.2 Reproducibility of Texture Features .....                                      | 10          |
| 1.3.4.3 Performance in BMD Measurements .....  | 11          |
| 1.4 Thesis overview and outline .....  | 11          |
| 1.4.1 Thesis statement .....   | 11          |
| 1.4.2 Outline .....  | 11          |
| <b>Chapter 2</b>   | <b>13</b>   |
| Methods .....  | 13          |
| 2.1 Novel Imaging Systems for In Vivo Studies of Bone .                                | 13          |
| 2.1.1 Ultra-High Resolution MDCT (UHR-MDCT) .....                                      | 13          |

|  |           |
|--|-----------|
| 2.1.2 Extremity Cone Beam CT(CBCT) .....   | 13        |
| 2.1.3 Pixelated Columnar CsI:TI Scintillator .....                                   | 14        |
| 2.2 Performance Evaluation in the Quantitative Assessment of Bone Health .....       | 16        |
| 2.2.1 Trabecular Microstructure Morphometry .....                                    | 16        |
| 2.2.2 Digital Topological Analysis (DTA) to Assess Rod and Plate<br>Morphology ..... | 19        |
| 2.2.3 Texture Analysis .....   | 24        |
| 2.2.4 CBCT Reconstruction and Bone Mineral Density Analysis .....                    | 27        |
| <b>Chapter 3</b> .....   | <b>30</b> |
| Performance Evaluation of UHR CT .....   | 30        |
| 3.1 Sources of Data and Imaging Protocols .....                                      | 30        |
| 3.2 Trabecular Morphometry .....   | 32        |
| 3.3 Radiomic Texture Features of Bone .....  | 35        |
| 3.3.1 Parameter Sweep .....  | 35        |
| 3.3.2 Texture Feature .....  | 37        |
| <b>Chapter 4</b> .....   | <b>40</b> |
| Performance Evaluation of CMOS-CBCT and FPD CBCT .....                               | 40        |
| 4.1 Sources of data, imaging protocols (including patient study) .....               | 40        |
| 4.2 Trabecular Morphometry .....   | 41        |
| 4.2.1 Derived Trabecular Metrics .....   | 44        |
| 4.3 Rods and Plate Morphology .....  | 45        |
| 4.4 BMD Reproducibility in CMOS-CBCT .....   | 46        |
| <b>Chapter 5</b> .....   | <b>49</b> |
| Future Directions: Pixelated Scintillators .....                                     | 49        |
| <b>Chapter 6</b> .....   | <b>50</b> |
| Discussion .....   | 50        |
| <b>Reference</b> .....   | <b>52</b> |
| <b>Vita</b> .....  | <b>55</b> |

# LIST OF TABLES

|  |    |
|--|----|
| Table 1: Comparison between NR-MDCT and UHR-MDCT .....           | 13 |
| Table 2: Comparison between FPD-CBCT and CMOS-CBCT systems ..... | 14 |
| Table 3: GLCM features equations .....                           | 25 |
| Table 4: GLRLM features equations .....                          | 25 |

# LIST OF FIGURES

Figure 1: Aquilion Precision CT..... 8

Figure 2: Extremity CBCT in weight-bearing(A) and unloaded(B) imaging configuration.... 8

Figure 3: Illustration of light spread in scintillators..... 9

Figure 3: Schematic of laser pixelated, micro-columnar CMS CsI:Tl (Left) and the edge profile of pixelated 675µm CMS CsI:Tl with a pixel pitch of 100µm..... 9

Figure 4: CMOS and FPD detector MTF measurements ..... 14

Figure 6: MTF results of ~700 µm thick CsI:Tl film, after pixilation (left) and after ALD coating. Zoom-in of the high-frequency range of the MTF showing 83% gain in contrast at Nyquist frequency ..... 15

Figure 7: Illustration of metrics for quantifying trabecular microstructure ..... 16

Figure 8: Illustration of the pipeline for obtaining trabecular morphometry..... 16

Figure 5: Illustration for ROI (white) selection in bone sample (left) and bone core (right) ... 17

Figure 10: Pseudocode Illustration of Bernsen segmentation..... 17

Figure 6: Pseudocode illustrating the primary thinning of the DTA algorithm ..... 19

Figure 7: Illustration of e-open (left) and v-open (right) points. (The red voxel represents the voxel of interests, the yellow voxel represents background, and the blue voxels represent the object) ..... 20

Figure 13: Illustration of rod-like 'Shape Point'. (The red voxel is the voxel of interest, background voxels in the yellow neighborhood should form a 6-closed path in (A), at least one voxel should be object in the blue neighborhood of (B) and yellow neighborhood of (C))..... 21

Figure 14: Illustration of plate-like 'Shape Point'. The yellow voxels and at least one of the green voxels should be background in the left figure. Each of the columns should contain at least one object voxel in the right figure..... 21

Figure 15: Illustration of Simple Point conditions. The red voxel represents the voxel of interest. The two 6-neighbor background points (yellow in the left figure) could form a 6-connected component through the 18-neighbor background point (blue voxel in the right)..... 21



|   |    |
|---|----|
| Figure 16: Illustration of e-open point deletion (for each of the three planes passing the voxel of interest (red), either all the yellow points in (A) are object points, or all the object points in the green neighborhood of (B) are 26-connected while not forming any tunnel. A tunnel is formed when all four green points are object points in(C))..... | 22 |
| Figure 17: Illustration of 'Thick Point'. For a point of interest (Red), the two green voxels should be background and blue voxel should be object in left figure, a pair of 26-connected blue points should be object points in the right figure.....  | 22 |
| Figure 18: Pseudocode for Final Thinning.....   | 22 |
| Figure 19: Illustration of a tunnel (A), e-points (B), and a cavity (the green voxels are object while center point is zero) (C) .....  | 23 |
| Figure 20: Illustration of GLCM and GLRLM matrix for (1,0) direction .....  | 24 |
| Figure 21: Illustration of GLCM and GLRLM texture features .....  | 26 |
| Figure 22: Pipeline for generating texture feature.....   | 27 |
| Figure 23: Illustration of BMD analysis pipeline.....   | 28 |
| Figure 24: Illustration of the ROIs for UHR-MDCT performance analysis .....   | 30 |
| Figure 25: Heatmap for the sweep study of reconstruction kernels and segmentation parameters for UHR-MDCT .....   | 31 |
| Figure 26: : Images of a human radius obtained by micro-CT, 50mAs UHR-MDCT (In-Air), 5mAs UHR-MDCT (In-Air), and NR (50mAs).....  | 32 |
| Figure 27: Matching ROI and Segmentation for Micro-CT, 50mAs (In-Air), 5mAs (In-Air), and NR (50mAs).....   | 32 |
| Figure 28: Correlation and difference plots of UHR-MDCT and NR-MDCT against micro-CT (at 50mAs).....  | 33 |
| Figure 29: Correlation of FC30 In-Body scan at exposures ranging from 375mAs to 25mAs with Micro-CT .....   | 34 |
| Figure 30: Illustration of FC30 In-Body scan at 375mAs and 50mAs .....  | 35 |
| Figure 31: Example plot used for visual examination of texture features as a function of the parameters of the texture extraction algorithm (here for the feature of Inverse .....  | 35 |
| Figure 32: Illustration of the ROIs for Texture Feature analysis in UHR MDCT.....   | 36 |
| Figure 33: Heatmap illustrating the correlation between texture features (UHR-CT and NR-CT) at 50mAs and texture features of UHR-CT at 100mAs .....   | 36 |

|   |    |
|---|----|
| Figure 34: Illustration of GLCM and GLRLM features (Energy, Entropy, and HGLRE) .....   | 37 |
| Figure 35: Correlation of texture feature between FC30 and other reconstruction kernels ....  | 37 |
| Figure 36: Concordance Correlation Coefficient of texture features between FC30 and other reconstruction kernels.....   | 38 |
| Figure 37: Axial slice showing the configuration of the 26 bone samples extracted from 4 cadaveric tibias used in the performance evaluation of CBCT (with BMD inserts) ..... | 40 |
| Figure 38: Example patient knee scan for BMD reproducibility analysis .....   | 41 |
| Figure 39: Trabecular metrics for aSi FPD-CBCT, CMOS-CBCT, and MDCT.....  | 41 |
| Figure 40: Difference plots (Bland-Altman-type) between the three modalities (CMOS-CBCT, aSi FPD-CBCT, and MDCT) and micro-CT plotted against the micro-CT metric value ..... | 42 |
| Figure 41: Correlations of derived metrics (Tb.Th and Tb.Sp) for CMOS-CBCT, aSi FPD-CBCT , and MDCT .....   | 43 |
| Figure 42: Illustration of the classification of rod-like and plate-like trabecular structures ....   | 45 |
| Figure 43: Visual Inspection of the thinning algorithm .....  | 45 |
| Figure 44: Correlation of CMOS and FPD Rod to Plate ratio against Micro-CT Rod to Plate ratio .....   | 45 |
| Figure 45: Classification result from Micro-CT, FPD, and CMOS.....  | 46 |
| Figure 46: : Illustration of ROIs for BMD reproducibility analysis in human subjects CMOS-CBCT .....  | 47 |
| Figure 47: Boxplot of ROI voxel values and a heatmap of mean ROI values for an example human subject dataset.....   | 47 |
| Figure 48: A scan of a human ulna obtained using Pixelated CMOS CSI:TI and conventional CT .....  | 49 |
| Figure 49: ROI comparison of Micro-CT and CMS CsI:TI with BvTv and TbTh correlation.  | 49 |

# Chapter 1

## *Introduction*

### **1.1.1 Significance**

Musculoskeletal conditions are a major concern among the world population. Millions of people suffer from bone-related diseases annually, especially in the elderly. A wide range of musculoskeletal conditions can affect bone health including osteoporosis (OP) and osteoarthritis (OA), which can significantly limit people's quality of life [1].

Bone mineral density (BMD), conventionally used for bone health assessment, can be measured reliably in conventional lower resolution CT to predict OP. However, BMD is a bulk measurement that reflects both the mineralization of bone and its microstructure [2]. Recent preclinical studies using ex-vivo and small-animal micro-CT (gold standard) show that independent assessment of bone microstructure might benefit early diagnosis of OA and OP. However, because of the small size of trabecular features ( $\leq 80\text{--}100\mu\text{m}$ ) [2], such assessment requires higher spatial resolution than is available on the current clinical x-ray modalities. Ongoing efforts to obtain quantitative assessment of trabecular microstructure in clinical settings also includes radiomic texture analysis. In this approach, intensity distribution patterns of small image neighborhoods provide indirect insights into the underlying microarchitecture.

Recently, new x-ray imaging systems with improved spatial resolution have been introduced, including ultra-high resolution multi-detector CT (MDCT) and flat-panel detector Cone Beam CT (CBCT). We evaluate whether these systems might enable direct quantitative

measurements of bone microstructure in clinical practice. The higher spatial resolution of these new modalities comes with potential trade-offs – for example, increased noise due to smaller detector pixels and scatter due to the use of large area flat-panel detectors in CBCT. Such tradeoffs could adversely affect BMD and texture measurement accuracy. Thus, there is a need for comprehensive technical evaluation of those new modalities across all metrics of bone health.

### **1.1.2 Osteoarthritis**

Osteoarthritis is a multifactorial condition that could be affected by factors such as genetic predisposition, aging, gender, and obesity. In 2010-2020, approximately 23% of adults in the US were diagnosed with arthritis and 10% showed arthritis-related limitation in activity, with numbers projected to increase [5]. The cascade of events that leads to OA is not currently well understood [3]. Cartilage loss and subchondral sclerosis is considered the main feature of late-stage OA [4]. The thinning of the subchondral plate and an increase in porosity and decrease in density of the underlying subchondral trabecular structure are the features of early-stage OA [4].

Research shows that factors such as joint alignment, the shape of articular bone surfaces, and bone microarchitecture are all intricately involved in the progression of OA [3]. Evidence shows that change in both the shape of the periarticular bone and the shape of the joint itself are responsible for initiating the OA process [3]. Compromising scenarios such as improper orientation and socket placement, and femoral head deviating from its spherical optimum (Cam type deformities) can cause abnormal contact within the joint, which may lead to high stresses on underlying bones [3]. These situations can eventually trigger the onset of OA. Microstructural changes such as sclerosis of the subchondral bone are also typical for OA [3]. Patients with severe OA show an increase of bone volume density and decrease in mineralization content [3].

Some studies, primarily in bone samples and animal models, suggests that cartilage loss and degeneration are preceded by subchondral bone alterations, such as thinning and increase in porosity in subchondral plate [3]. Further animal model studies using micro-CT are still underway to discover information about the cascade of events in OA [3]. Due to the multifactorial nature of the disease, the cascade of events is likely different from human to animal and even between patient populations [3]. Thus, new imaging technology is needed to translate the pre-clinical findings regarding the role of subchondral microarchitecture in OA to comprehensive patient studies [3].

### **1.1.3 Osteoporosis**

Osteoporosis is the condition where bone mass drops to a level below which the likelihood of fracture dramatically increases. OP and OP-related fractures are a major health concern. It is estimated that around 40% of white women older than 50 years old and around 13% of men will experience an osteoporosis-related fracture [6]. In 2005, the cost for OP-related fractures were around 13 to 20 billion dollars and is projected to keep rising [6].

Osteoporosis is caused by imbalance of bone resorption and formation, commonly influenced by endogenous hormone change and external mechanical load [7]. Such factors can take effect through the activities of bone cells such as osteoblasts (deposition) and osteoclasts (resorption) [7]. The amount and proportion of the two cells directly influence bone strength [7]. Bone mass peaks at age 16-25 and then gradually reduces, typically faster in women than in men [7]. Women lose significantly more bone mass during the first 5 years of menopause [7]. Type 1 osteoporosis is related to the onset of menopause [7]. The primary osteoporosis related to aging is classified as Type 2. Different from Type 1, which only affects cancellous bone, Type 2

osteoporosis affects both cancellous and cortical bone [7]. This makes Type 2 OP patients more susceptible to cortical bone fracture [7]. On top of normal aging, factors such as dietary calcium deficiency, and lower physical activity all promote bone resorption and inhibit bone formation [7].

While OP is typically diagnosed by a measurement of BMD, the underlying bone loss is associated with changes in bone microstructure. Normal cancellous bones have interconnected horizontal and vertical trabeculae. This structure provides great compressive strength [7]. However, cancellous bones have the tendency to lose horizontal trabeculae, which reduce the interconnected scaffolding [7]. This could cause the unconnected trabeculae to easily break under minor load [7]. Cortices of long bones have a compensatory mechanism to counteract the decrease in bone mass, which results in mid-shaft of long bones being more resistant to age-related fracture. This, however, does not apply to the vertebral column since the cortical shell only accounts for 10% of bone strength. Therefore, bone microarchitecture might provide an additional predictor of susceptibility to OP fracture to augment the current BMD-based evaluation. These findings underscore the need for improved assessment of trabecular microarchitecture in OP.

## **1.2 Quantitative Assessment of Bone using X-ray Imaging**

### **1.2.1 Bone Mineral Density (BMD)**

X-ray imaging measures the attenuation encountered by an x-ray beam in the object [8]. In CT, multiple x-ray views are acquired around the object and a reconstruction algorithm is used to obtain a map of the x-ray attenuation coefficient. Volumetric BMD of the object can then be

inferred from the attenuation coefficient [9] by using calibration phantoms with known bone mineral concentrations. Such measurements are typically obtained from conventional single energy CT, although a more accurate assessment could be achieved with dual-energy CT that can account for the presence of fat in yellow marrow [9]. (Note that an alternative approach for BMD estimation involves measurements of areal BMD from Dual Energy X-ray Absorptiometry, DXA. This technique remains the mainstay of clinical assessment of OP, although it suffers from biases due to tissue superposition inherent to 2D imaging.)

A BMD test is clinically used to identify osteoporosis, predict fracture risk, and measure the response to osteoporosis treatment [10]. The test produces a score comparing the measured mineral density to an established norm [10].

## **1.2.2 Radiomic Texture Analysis**

Recent publications have introduced radiomic imaging features as feasible biomarkers for clinical use [11] [12]. Radiomics typically operates on large databases of clinical images to identify combinations of quantitative image features – including various metrics of texture – that are predictive of a disease state.

In this thesis, we investigate the application of radiomic texture features of bone. By converting medical images into quantitative attributes, texture analysis could potentially provide a noninvasive characterization that accounts both for the large-scale density distribution of bone and its small-scale microarchitecture [11]. Using texture analysis, changes in trabecular microstructure can potentially be detected (although not directly measured), which could in turn be used as a predictor of bone strength [13] [14]. Research has shown that texture features from CT are predictive of vertebral failure load [14].

### **1.2.3 Measurement of Trabecular Morphometry**

In this approach, direct measurements of the morphology of the trabecular lattice are obtained. As discussed earlier, the applications of morphometry are typically limited to pre-clinical micro-CT because of the need for high spatial resolution. The analysis begins with a segmentation step to separate the trabeculae from background. A global threshold is generally sufficient for micro-CT to achieve accurate segmentation, while more sophisticated segmentation methods modulating the threshold based on local neighborhood are needed for systems with lower spatial resolution [16]. Bone morphometry features including bone volume fraction (BvTv), trabecular thickness (Tb.Th), and trabecular separation (Tb.Sp) are then computed in regions of interest (ROIs) using a sphere fitting algorithm [17].

Studies demonstrate the relation of morphometric parameters to progression of OA and OP. In multiple animal models for OA, an increase in Tb.Sp, and a decrease in BvTv and Tb.Th in subchondral trabecular bone were detected [4]. For OP, it is known that age-related degradation of trabecular structure includes morphological changes such as decrease in Tb.Th, increase in Tb.Sp and loss in connectivity [15].

### **1.2.4 Individual Trabecular Segmentation (ITS) to Assess Rod and Plate Morphology**

Within the framework of trabecular morphometry, structure model index (SMI) is used to estimate the plate or rod characteristic of the trabecular bone (from 0 being ideal rod to 3 being ideal plate) [18]. Research shows that plate-like structure contributes more substantially to the elastic behavior of bone than rod-like structure does. For hip fracture in osteoporosis, there is a



preferential loss of plate-like trabecular structure, which leads to compromised mechanical competency [19]. Other study shows that a more plate-like structure of the trabecular bone leads to a reduction in fracture risk [19]. Furthermore, a dramatic change from plate-like to rod-like of trabeculae was found to be associated with aging and osteoporosis [18].

Trabecular morphometry provides global characterization of the overall contributions of rods and plates to the trabecular lattice. An emerging methodology based on individual trabecular segmentation (ITS) attempts to classify each trabecula as being rod- or plate-like. This approach includes skeletonization and topological classification. A segmented trabecular bone image is first transformed into a collection of 1-voxel-thick curves and surfaces; each resulting voxel is then identified by a corresponding topological type (e.g. surface, curve, junction). Using the classified skeleton representation, the original trabecular bone image is reconstructed with rod-like and plate-like structures identified. Plate-to-Rod ratio is Plate bone volume divided by Rod bone volume [19].

### **1.3 Emerging Modalities for Bone Imaging**

Currently, quantitative CT (QCT) by conventional MDCT is used to measure BMD for bone health monitoring. However, the application of current generation MDCT to compute the metrics of trabecular micro-architecture (~50-200  $\mu\text{m}$  in size) is challenging due to its limited spatial resolution (~250-300  $\mu\text{m}$ ) [16]. This thesis focuses on the following new technologies, which could potentially lead to better imaging performance in quantitative evaluation of bone microstructure.

### 1.3.1 Ultra-High Resolution MDCT (UHR-MDCT)

UHR-MDCT scanners such as the Somatom Force (Siemens) and Aquilion Precision (Canon, shown in Fig. 1), with smaller focal spot size and voxel size than current-generation MDCT have recently been introduced.

UHR-MDCT can achieve up to 2 times higher spatial resolution compared to current standard CT (250–300

$\mu\text{m}$ ) [20]. This technology enables the visualization of details down to 150  $\mu\text{m}$  [20]. As visualization capability approaches the size of trabeculae, improved quantification of trabecular structure could potentially become possible.



**Figure 8:** Aquilion Precision CT ( us.medical.canon)

### 1.3.2 Extremity Cone Beam CT (CBCT)

CBCT systems investigated here are based on Onsite 3D extremity scanner (Carestream Health, Rochester NY) [16]. This system (Fig. 2) has the advantage of being able to perform both volumetric weight-bearing and unloaded extremity imaging [16].

Furthermore, it uses an amorphous Silicon (aSi) Flat Panel Detector (FPD) that offers

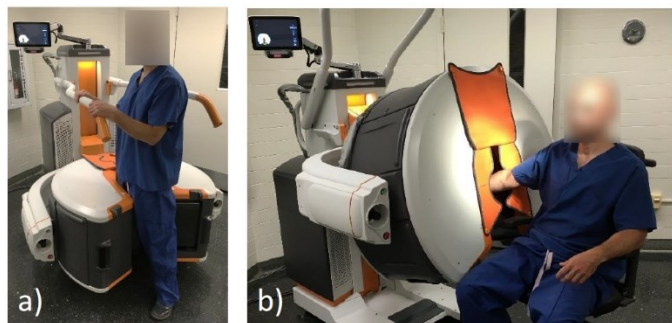


**Figure 9:** Extremity CBCT in (a) weight-bearing and (b) unloaded imaging configurations [16]

improved spatial resolution compared to the current MDCT, owing to its smaller pixel size of  $\sim 150 \mu\text{m}$  [16]. Recently, a new configuration of the CBCT system that replaced the aSi FPD with a custom Complementary metal–oxide–semiconductor (CMOS) detector was also investigated [16]. With an even smaller detector pixel size, higher frame rate, and lower

electronic noise, the CMOS detector can further enhance the performance of the extremity CBCT system [16] in high-resolution imaging tasks such as quantitative assessment of bone microstructure.

### 1.3.3 Pixelated Columnar CsI:Tl Scintillator

In conventional CT and CBCT detectors, x-ray energy is converted to light in a scintillator, where x-rays interact with a scintillation material through the photoelectric effect. The photoelectron produced through the photoelectric effect de-excites and produces light, which is subsequently converted to electrical current through the attached photo-diode [8]. Traditionally, trade-off exists between the thickness of the scintillator and the resulting resolution, with thicker scintillators providing better absorption (from increased probability of photon interaction within the longer path along the scintillating material) but reduced spatial resolution due to scintillation light spread, and vice versa (Fig. 3).

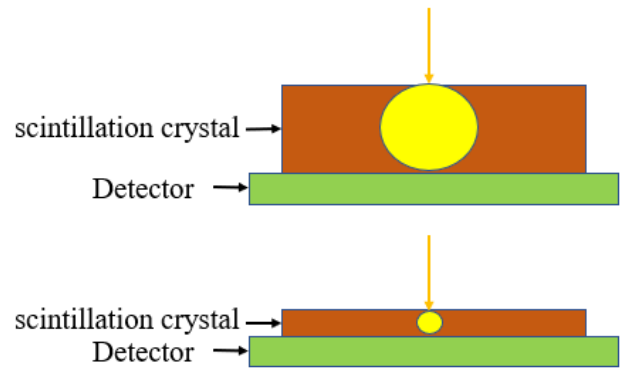


**Figure 3:** Illustration of light spread in scintillators

A newly developed pixelated columnar CsI:Tl scintillator (Fig. 4) for the previously mentioned extremity CMOS CBCT can reduce light spread due to light channeling inside the laser-cut pixels, offering improved spatial

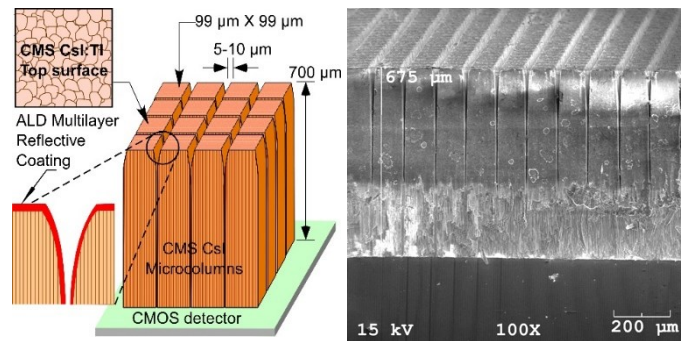


**Figure 10:** Schematic of a laser pixelated, micro-columnar CMS CsI:Tl and the edge profile of pixelated 675 μm CMS CsI:Tl with a pixel pitch of 100 μm [2]

resolution and contrast. The new scintillator technology, combined with the previously mentioned CMOS technology, could provide an even greater improvement in resolution from current standard MDCT while having low electronic noise, which benefit the accuracy and reproducibility of trabecular measurements.

### **1.3.4 Performance Assessment**

With resolution approaching the size of trabeculae, the systems mentioned above could potentially enable the individual morphometric measurement of trabecular microstructure and could in turn generate biomarkers to facilitate a better understanding, prognosis, and assessment of OP, OA, and other bone diseases. Thus, the performance of the above systems is analyzed in this thesis for their ability to address the current challenges faced in trabecular measurements.

#### ***1.3.4.1 Trabecular Morphometry***

The above-mentioned emerging high-resolution imaging modalities were assessed in terms of correlation and quantitative agreement of trabecular morphometry with gold standard micro-CT to determine if their resolution is sufficient to enable robust, direct detection of pathological changes in bone microstructure.

#### ***1.3.4.2 Reproducibility of Texture Features***

For texture analysis, which could be performed by both the current generation CT and the new high-resolution modalities, the higher resolution CT could potentially affect local image texture, thus influencing the resulting texture features. This could make the established texture analysis pipeline developed for current MDCT inappropriate for the new CT modalities. Thus,

we evaluated the agreement between texture features generated using the new CT modalities and the texture features from current standard MDCT.

#### ***1.3.4.3 Performance in BMD Measurements***

CBCT has the advantage of isotropic resolution and volumetric coverage without translation. However, the latter advantage is associated with increased x-ray scatter that may result in cupping and streak artifacts. This could adversely affect quantitative accuracy of BMD measurements. Thus, it is also necessary to assess the performance of new CT modalities in BMD evaluation.

## **1.4 Thesis Overview and Outline**

### **1.4.1 Thesis Statement**

Technical performance evaluation of the emerging high-resolution x-ray imaging systems, specifically UHR-MDCT and CMOS-based CBCT, indicates that this new generation of clinical scanners provides improved in vivo assessment of human bone micro-structure compared to the current systems, while maintaining the capability for application of established bone biomarkers of BMD and radiomic texture features.

### **1.4.2 Outline**

Chapter 2 details the technical specifications of the previously mentioned high-resolution imaging technologies and introduces the biomarkers considered in the performance evaluation studies. Implementation details of a general pipeline for generating each biomarker are

discussed. Model-based algorithms for quantitatively accurate reconstruction of CBCT human subject data are also introduced in this chapter.

Chapter 3 presents the performance evaluation of Ultra-High-Resolution MDCT (UHR-MDCT) and Chapter 4 presents the evaluation of CMOS-CBCT and aSi FPD-CBCT. In addition to the results of the performance evaluations, we discuss the procedures for registration of the scan volumes to ground truth micro-CT, for placement of Region of Interests (ROIs) for biomarker measurements, and for optimization of the settings of the biomarker measurement algorithms.

Chapter 5 discusses the future directions for development of imaging systems for quantitative bone imaging, specifically by using pixelated scintillators. The performance of a CMOS detector with a pixelated scintillator is evaluated in terms of trabecular morphometry. A general summary and discussion of the investigations presented in the thesis is provided in Chapter 6.

# Chapter 2

## *Methods*

### 2.1 Novel Imaging Systems for In Vivo Studies of Bone

The following section lay out in detail the technical specification of the high resolution imaging modalities that are investigated in this thesis.

#### **2.1.1 Ultra-High Resolution MDCT (UHR-MDCT)**

The high-resolution MDCT system (UHR-MDCT), with reduced focal spot size (0.4×0.5 mm) and ~150 μm pixel size, has been reported to deliver ~2× improved spatial resolution compared to conventional MDCT. The two protocols listed in Table 1 were used for imaging: Ultra High Resolution acquisition and Normal Resolution, which represents current generation MDCT [16].

#### **2.1.2 Extremity Cone Beam CT (CBCT)**

The aSi FPD and CMOS-CBCT systems were based on the Onsite3D extremity scanner, which was designed to enable weight bearing imaging in a natural stance [16]. The

gantry accommodates source and detector motion around the patient leg, and, by changing the height

**Table 5:** Comparison between NR-MDCT and UHR-MDCT [16]

|                                | NR-MDCT         | UHR-MDCT        |
|--------------------------------|-----------------|-----------------|
| <b>Nominal CTDI Dose</b>       | 10.8 mGy        | 10.8 mGy        |
| <b>Scan Time</b>               | 2.0 secs        | 2.7 secs        |
| <b>Focal Spot Size</b>         | 0.8 mm x 1.3 mm | 0.4 mm x 0.5 mm |
| <b>Detector Channels</b>       | 896 channels    | 1796 channels   |
| <b>Number of detector rows</b> | 80 rows         | 160 rows        |
| <b>Slice Thickness</b>         | 0.5 mm          | 0.25 mm         |
| <b>Voxel Size (in-plane)</b>   | 0.053 mm        | 0.0133 mm       |

and gantry angulation, can also be used for unloaded upper or lower extremity imaging [16]. The difference between the two imaging systems is summarized in Table 2. While the aSi FPD already offers a substantial improvement in resolution compared to current MDCT due to smaller detector pixels, the CMOS detector provides a higher frame rate, smaller pixels, and lower electronic noise. With its smaller pixel size and reduced scintillator thickness, CMOS-CBCT achieved higher resolution compared to aSi FPD-CBCT. This improvement in performance can be visualized through the modulation transfer function (MTF) plot in Fig. 5, which shows a  $\sim 1.2\times$  improvement in the limiting frequency (MTF at 10%) of CMOS-CBCT compared to aSi FPD.

|                               | FPD-CBCT                         | CMOS-CBCT                        |
|-------------------------------|----------------------------------|----------------------------------|
| <b>Detector</b>               | Varex PaxScan2530<br>a-Si FPD    | Dalsa Xineos3030<br>CMOS         |
| <b>Pixel Size</b>             | 139 $\mu\text{m}$                | 99 $\mu\text{m}$                 |
| <b>Scintillator Thickness</b> | $\sim 0.7$ mm                    | $\sim 0.4$ mm                    |
| <b>e- Noise</b>               | $\sim 2000$ e-                   | $\sim 140$ e-                    |
| <b>Frame Rate</b>             | Up to 7.5 fps (full res.)        | Up to 30 fps (full res.)         |
| <b>X-ray Source</b>           | Three Source<br>Stationary Anode | Single source,<br>Rotating Anode |
| <b>Focal Spot</b>             | 0.5                              | 0.3                              |

**Table 6:** Comparison between FPD-CBCT and CMOS-CBCT systems [16]

### 2.1.3 Pixelated Columnar CsI:TI Scintillator

Microcolumnar CsI:TI scintillator screens are widely used as they offer an advantageous trade-off between detection efficiency vs. spatial resolution owing to partial light channeling in the microcolumns [2]. However, microcolumnar CsI:TI scintillator screens still suffer from the lateral light spread which limits system resolution through the resulting blur [2].

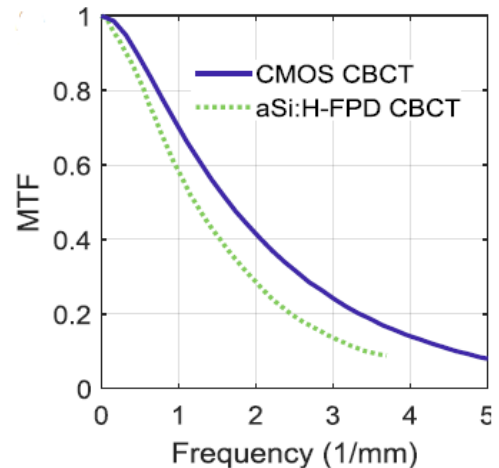


**Figure 5:** CMOS and FPD detector MTF measurements [15]



A recently developed pixelated columnar CsI:TI scintillator employs micro-machined detector pixels to reduce light spread to the dimension of the detector pixels. This, in turn, improves resolution without the need to use thinner scintillators, thereby minimizing the reduction in x-ray absorption. In our studies, we used a laser-machined high crystallinity CsI:TI film [2]. Atomic layer deposition (ALD) coating was applied to prevent light from crossing into surrounding pixels [2]. After the laser treatment, a loss in resolution was initially observed (Fig. 6). However, after the application of ALD coating, the resulting samples showed a ~47% increase in resolution, a 77% gain in contrast, and an 83% gain in contrast at Nyquist frequency compared to an unpixelated detector of the same thickness [2].

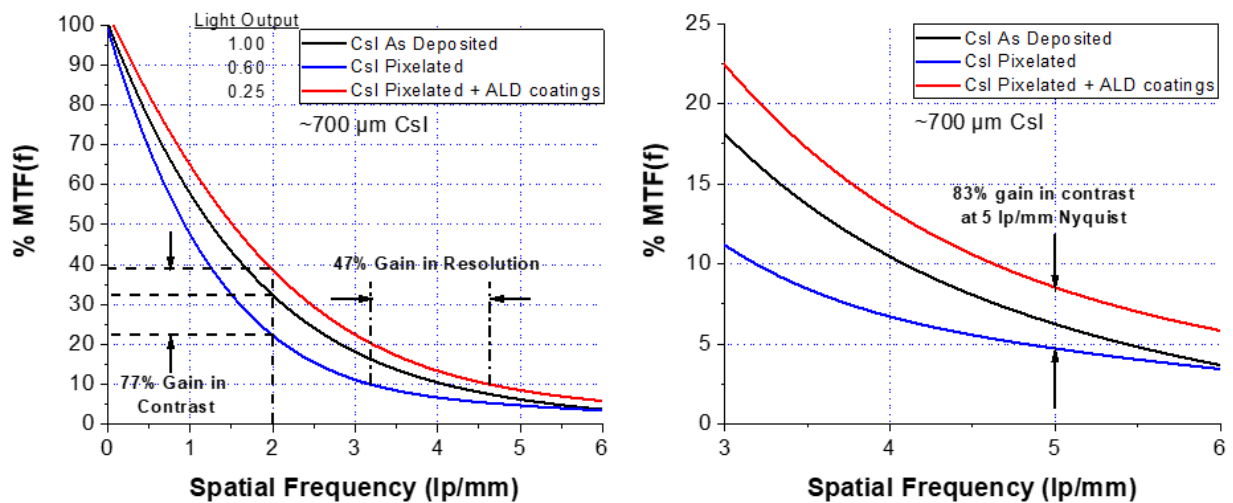


**Figure 6:** MTF results of ~700 μm thick CsI:TI film, after pixilation (left) and after ALD coating. Zoom-in of the high-frequency range of the MTF showing 83% gain in contrast at Nyquist frequency [2].

## 2.2 Performance Evaluation in Quantitative Assessment of Bone Health

### 2.2.1 Trabecular Microstructure Morphometry

The four trabecular structure metrics illustrated in Fig. 9 were used: BvTv; Tb.Th; Tb.Sp; and Tb.N. BvTv is the fraction of the mineralized bone voxel to the total number voxels in an ROI. Tb.Th measures the thickness of a segmented trabecular ridge. Tb.Sp measures the spacing between the trabecular ridges. The Tb.Th and Tb.Sp computations use a sphere fitting algorithm [21]. Tb.N is the inverse of the distance between mid-axis of segmented trabeculae. The Tb.Th, Tb.Sp, and Tb.N values used in the performance evaluation below represent the mean of the non-zero measurements within the ROI (mean of yellow/red area in Fig. 7) [22].

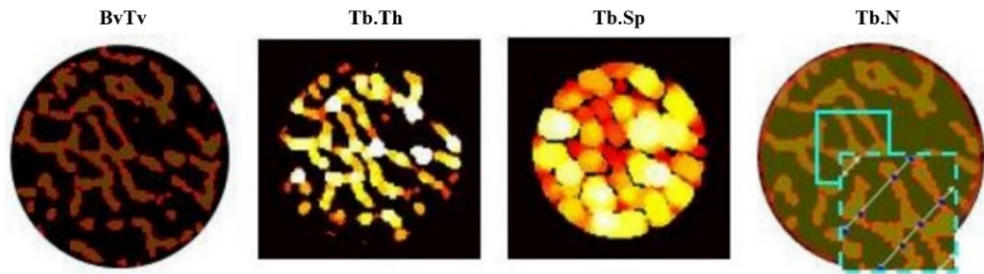


**Figure 7:** Illustration of metrics for quantifying trabecular microstructure [16]

computations use a sphere fitting algorithm [21]. Tb.N is the inverse of the distance between mid-axis of segmented trabeculae. The Tb.Th, Tb.Sp, and Tb.N values used in the performance evaluation below represent the mean of the non-zero measurements within the ROI (mean of yellow/red area in Fig. 7) [22].

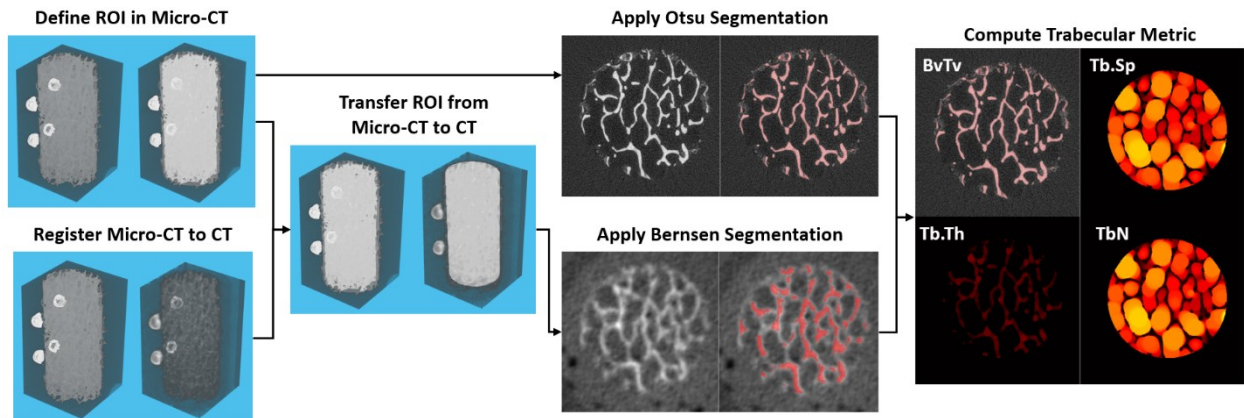


**Figure 8:** Illustration of the pipeline for obtaining trabecular morphometry.

We used human bone samples for evaluation of trabecular morphometry. Fig.8 illustrates the pipeline for generating trabecular measurements from scan data. A micro-CT scan of the bone sample was used as the ground truth. The ROIs for subsequent analysis were first defined in each of the Micro-CT volumes as a binary mask (Fig. 9). To locate the same ROI in bone scans obtained on the other CT systems, each micro-CT bone volume was registered to a CT scan of the same bone sample using MITK. ROIs generated in the micro-CT volume were then transferred to the corresponding scan volumes using a transformation matrix obtained through the registration step. As a result, the same set of ROIs could be placed in the scans of a particular bone for all CT systems under investigation.

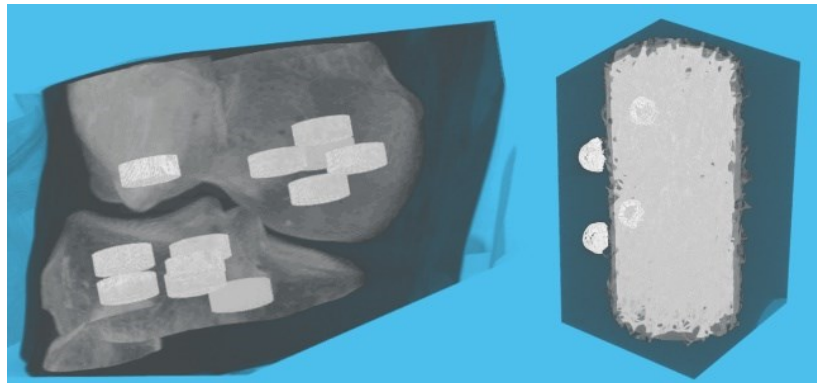


**Figure 11:** Illustration for ROI (white) selection in bone sample (left) and bone core (right)

Segmentation was applied to all cropped ROIs to delineate the trabecular structure from the background. For micro-CT, which has high resolution, MITK's Otsu segmentation was used. Otsu's method generates a binary image from the original grey level image by finding the threshold value that maximizes inter-class variance and minimizes intra-class variance. For CT scans with limited resolution, such as the images obtained from

```

if 'local contrast' is less than 'contrast threshold'
  if 'mid gray' is greater than 128
    voxel = 1
  else
    voxel = 0
  end
else
  if 'pixel value' is larger than 'mid gray'
    Voxel = 1
  else
    Voxel = 0
  end
end

```

**Figure 10:** Pseudocode Illustration of Bernsen segmentation [23]

CBCT and MDCT, Bernsen's thresholding was used. Before applying the Bernsen's segmentation, all volumes were converted to 8-bit.

Bernsen's thresholding has two user defined parameters: radius and contrast threshold [23]. For each voxel in the volume, a square local neighborhood with size defined by the user specified radius variable was used to generate two values:

$$\text{Local contrast} = \text{local maximum} - \text{local minimum}$$

$$\text{Local mid gray} = (\text{local minimum} + \text{local maximum})/2$$

Fig. 10 outlines the pseudocode of Bernsen's segmentation. The user-selected contrast threshold considers the intensity difference in a neighborhood of a voxel. Below the threshold, the neighborhood is considered uniform and the voxel is assigned to the class of the entire neighborhood. This method can therefore effectively ignore minor local intensity changes due to blur or artifacts. For neighborhoods exhibiting more contrast than the threshold, the voxel class is determined by comparing the voxel value with the mid gray value of the neighborhood. Previous studies in CBCT showed that a global pre-threshold before Bernsen segmentation helps in removing background noise and tissue, and facilitates better delineation of trabecular structures [16].

A previously developed framework [22] used to generate trabecular metrics for each ROI. However, the previous implementation cropped the ROI-masked volume before computing the metric – i.e. any voxel outside of the mask was assigned a zero value. Since the code uses a sphere fitting algorithm, this could cause the value of the metrics to be erroneously calculated in areas adjacent to the ROI boundary. Specifically, a continuous trabecular structure would be showing an artificial sharp edge at the ROI boundary. To avoid the inaccurate calculation at the

edge of the ROI, in this thesis we chose a different approach. Instead of cropping the segmented volumes before computing the metric, we cropped the volumes containing the local morphological measurements before obtaining their mean values for the analysis, but after segmentation.

The metric values from the different modalities were then correlated with the ground truth values obtained from micro-CT to assess imaging performance. In order to find the optimal Bernsen segmentation settings, a parameter sweep for radius and contrast threshold was conducted. The parameters that yielded the best correlation with micro-CT were used.

## 2.2.2 Digital Topological

### Analysis (DTA) to Assess

### Rod and Plate

### Morphology

In addition to the conventional geometric measurements, we also considered the metric of Rod to Plate ratio. As mentioned in the introduction, the proportion of Rod-like to Plate-like structures correlates with bone strength and fracture risk.

```

Set all voxel with value equals to 1 to 0
Set all voxel with value equals to 0 to -1000

Iteration = 0
while voxels are being deleted in the previous iteration
    Iteration = Iteration + 1
    Threshold = -1000 + Iteration
    for each of the 8 sub-field
        scan for s-open, e-open, and v-open points in the sub-field
        if an s-open point equal to 0
            if the s-open point is 'Shape Point'
                the s-open point = Iteration
            else if the s-open point is 'Simple Point'
                the s-open point = Threshold
            end
        end
        if an e-open point equal to 0
            if the e-open point is 'Simple Point'
                if the e-open point Satisfy 'delete condition for e-open point'
                    the e-open point = Threshold
                end
            end
        end
        if a v-open point equal to 0
            if the v-open point is 'Simple Point'
                the v-open point = Threshold
            end
        end
    end
end
end
end
end

```

**Figure 12:** Pseudocode illustrating the primary thinning of the DTA algorithm

Digital topological analysis (DTA) involves skeletonization and topological classification. The shape preserving parallel thinning algorithm proposed by Saha et. Al. [24] was implemented for skeletonization. As a result, the segmented trabecular bone image (see Section 2.2.1) was transformed into 1-voxel-thick curves and surface skeletons, where the curve represented the rod-like structures and the surface represented the plate-like structures in the trabeculae.-like structures and surface represented the plate-like structures in the trabeculae.

The skeletonization procedure iteratively removes surface voxels from the original binary volume and saves voxels that are integral to the structure until the original volume is reduced to a skeleton. The algorithm (Fig. 10) is able to

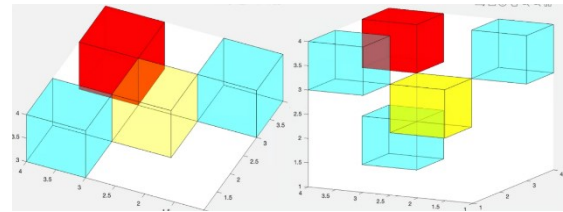


**Figure 13:** Illustration of e-open (left) and v-open (right) points. (The red voxel represents the voxel of interests, the yellow voxel represents background, and the blue voxels represent the object)

track the voxels deleted and saved as part of the final skeleton in each iteration, so the skeleton volume can be traced back to the original form. Before the iterations, object voxels are set to 0 and background voxels to  $-1000$ . At each iteration, the iteration number is tracked. A threshold value is computed, which is then assigned to the points deleted in that iteration. As the algorithm progress, points saved or deleted in each iteration have a unique identifier, with voxels smaller than 0 always belonging to the background. Since the algorithm processes each of the surface points based on its  $3 \times 3$  neighborhood, under some circumstances two connected voxels could both satisfy the condition for deletion in an iteration. However, it would break the structural connectivity if both were deleted. To avoid this situation, the volume is processed as eight sub-fields, such that no two voxels within each sub-field are 26 connected.

The skeletonization has two steps: primary and final thinning. The primary thinning iteratively removes surface voxels from the binary volume

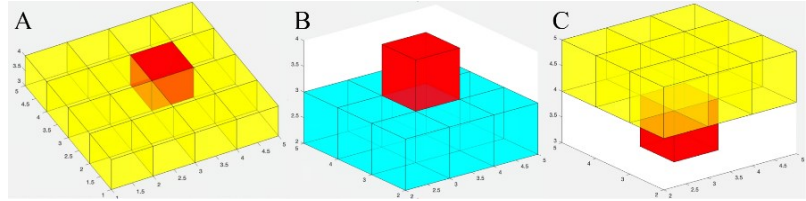


**Figure 13:** Illustration of rod-like 'Shape Point'. (The red voxel is the voxel of interest, background voxels in the yellow neighborhood should form a 6-closed path in (A), at least one voxel should be object in the blue neighborhood of (B) and yellow neighborhood of (C))

(Fig. 11). In each iteration, the voxels in the current outer shell of the object are identified as s-open points (object point with one 6-connected background point), e-open points, or v-open points (Fig. 12 for neighborhood voxel composition).

The identified voxels will be saved if they are structurally integral (shape points). Shape points can be classified either as a rod-like or a plate-like structure. A rod-like structure should, in one dimension, be 6-closed path by background, and have two object points extended one from each end (Fig. 13). A plate-like structure should be one to two-voxel thick in one dimension and have at least one 26-connected point in each of the orthogonal directions (Fig. 14).

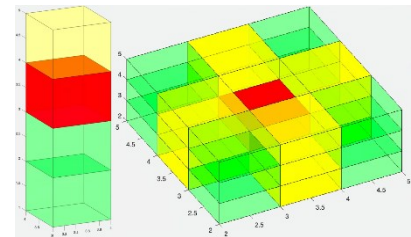


**Figure 14:** Illustration of plate-like 'Shape Point'. The yellow voxels and at least one of the green voxels should be background in the left figure. Each of the columns should contain at least one object voxel in the right figure

The identified voxels will be deleted if they are 'simple points'. A voxel needs to satisfy four conditions to be considered 'Simple Point': (1) have at least one 26-neighbor object point; (2) have at least one 6-neighbor background point;

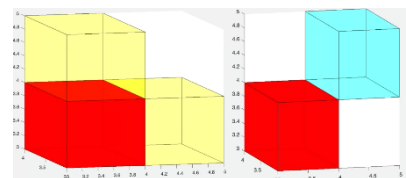


**Figure 15:** Illustration of Simple Point conditions. The red voxel represents the voxel of interest. The two 6-neighbor background points (yellow in the left figure) could form a 6-connected component through the 18-neighbor background point (blue voxel in the right)







algorithm proposed by Saha et. al. was used for classifying each of the resulting skeleton points [25]. Each of the object points was classified based on the voxel arrangement of its neighborhood points.

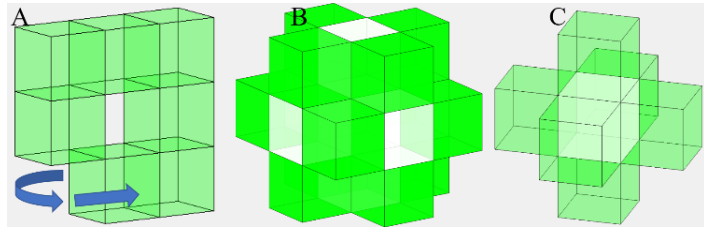


**Figure 19:** Illustration of a tunnel (A), e-points (B), and a cavity (the green voxels are object while center point is zero) (C)

The 3-by-3 neighborhood around the point of interest were extracted, and the central point was set to zero. Three attributes were computed to classify each point: the number of tunnels, number of 26-components, and the number of cavities (Fig. 19).

To find the number of tunnels for one voxel, all 18-neighbors background voxels were first isolated. The number of 6-connected components were found in the group of background points. The number of tunnels was 1 minus the number of 6-connected components that also contained a 6-neighbor background point.

All skeleton voxels were first classified into 9 groups based on the composition of their object 6-neighbors. For a voxel's neighborhood, if a 6-connected point belongs to the object, the surface that it belongs to could be ignored, since the class of other point on the surface would not affect the computation of the attribute. The same is true for e-points (Fig. 16 B): if an e-point belongs to the object, the edge that it belongs to could be ignored. Thus, for number of 26-component, the attribute could instead be formulated as the number of object 26-component in the remaining neighborhood. Due to the limited variation that the remaining voxels exhibit after ignoring surfaces and edges, and the fact that an attribute computed from one orientation of the voxel composition is applicable in different orientations, a lookup table was generated in which the 3 attribute numbers were generated for all voxel compositions in each of the nine classes.

By applying the lookup table to all skeleton voxels, each skeleton voxel was assigned a set of three attribute values. Using a predefined lookup table [25] that matched the attribute value to a topological voxel type, each voxel was categorized into 1 of the 8 voxel types. Voxel type includes edge point of surface, inner point of surface, junction point of surface, junction point of surface and arcs, arc end point, inner point of arc, junction point of arcs, and isolated point.

The algorithm was implemented such that the resulting skeleton volume contained the information about all the points that had been deleted in each iteration. Thus, it is possible to return the skeleton back to the original structure layer by layer. To approximate the rod and plate structure in the original volume, all the arc points were assigned a value of 1, all surface points were assigned a value of 2, and all junction points were assigned a value of 1.5. For each added layer, each of the voxels would assume the mean of its existing object voxel neighbors as the value. When all the points were added back, a threshold was applied to the whole volume, and voxels with values larger than 1.5 were classified as plate-like structures. Voxels with value larger than 0 and smaller than 1.5 were classified as rod-like structures. Plate to Rod ratio was then computed as the number of plate voxels divided by the number of rod voxels [26].

### 2.2.3 Texture Analysis

Texture features were extracted and analyzed for different imaging protocols. The original scans were converted to 8-bit grayscale

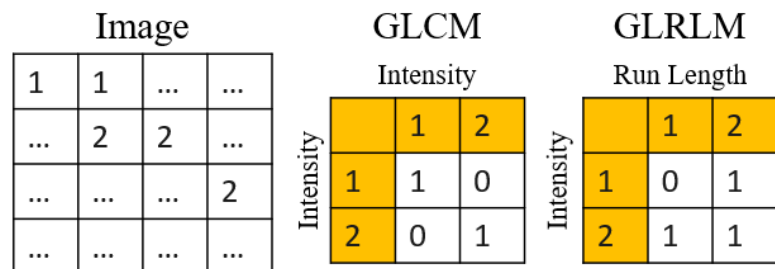


Figure 20: Illustration of GLCM and GLRLM matrix for (1,0) direction

volumes for texture analysis. Digital masks were generated to identify bone samples in the scans.

A set of 403-voxel ROIs were generated within each bone mask. Within each dataset, the bone sample scans from different imaging protocols were aligned at the same orientation. For situations where the same bone was imaged in different orientations or on different scanners, the bone masks were first registered, and the ROIs were then regenerated for each dataset.

**Table 7:** GLRLM features equations [27]

| GLRLM Features                             | Equation  |
|--|---|
| Short run emphasis (SRE)                   | $f_1 = \frac{\sum_{i,j} \frac{g(i,j)}{j^2}}{\sum_{i,j} g(i,j)}$     |
| Long run emphasis (LRE)                    | $f_2 = \frac{\sum_{i,j} g(i,j)j^2}{\sum_{i,j} g(i,j)}$              |
| Grey level non-uniformity (GLN)            | $f_3 = \frac{\sum_i (\sum_j g(i,j))^2}{\sum_{i,j} g(i,j)}$          |
| Run length non-uniformity (RLN)            | $f_4 = \frac{\sum_j (\sum_i g(i,j))^2}{\sum_{i,j} g(i,j)}$          |
| Low grey level run emphasis (LGRE)         | $f_5 = \frac{\sum_{i,j} \frac{g(i,j)}{i^2}}{\sum_{i,j} g(i,j)}$     |
| High grey level run emphasis (HGRE)        | $f_6 = \frac{\sum_{i,j} g(i,j)i^2}{\sum_{i,j} g(i,j)}$              |
| Short run low grey level emphasis (SRLGE)  | $f_7 = \frac{\sum_{i,j} \frac{g(i,j)}{i^2 j^2}}{\sum_{i,j} g(i,j)}$ |
| Short run high grey level emphasis (SRHGE) | $f_8 = \frac{\sum_{i,j} \frac{g(i,j)i^2}{j^2}}{\sum_{i,j} g(i,j)}$  |
| Long run low grey level emphasis (LRLGE)   | $f_9 = \frac{\sum_{i,j} \frac{g(i,j)j^2}{i^2}}{\sum_{i,j} g(i,j)}$  |
| Long run high grey level emphasis (LRHGE)  | $f_{10} = \frac{\sum_{i,j} g(i,j)i^2 j^2}{\sum_{i,j} g(i,j)}$       |

A remote module for Insight Toolkit named itkTextureFeatures was used to generate texture feature maps from the CT scan volumes [27]. Co-occurrence features were generated from the grey level co-occurrence matrix (GLCM) for each voxel's neighborhood. Similarly, run length features were generated based on the grey level run length matrix

**Table 8:** GLCM features equations [27]

| GLCM Features             | Equation  |
|---------------------------|---|
| Energy                    | $f_1 = \sum_{i,j} g(i,j)^2$   |
| Entropy                   | $f_2 = \begin{cases} \sum_{i,j} g(i,j) \log_2 g(i,j) & \text{if } g(i,j) \neq 0 \\ 0 & \text{if } g(i,j) = 0 \end{cases}$ |
| Correlation               | $f_3 = \sum_{i,j} \frac{(i-\mu)(j-\mu)g(i,j)}{\sigma^2}$  |
| Inverse Difference Moment | $f_4 = \sum_{i,j} \frac{1}{1+(i-j)^2} g(i,j)$   |
| Inertia/Contrast          | $f_5 = \sum_{i,j} (i-j)^2 g(i,j)$   |
| Cluster Shade             | $f_6 = \sum_{i,j} ((i-\mu) + (j-\mu))^3 g(i,j)$   |
| Cluster Prominence        | $f_7 = \sum_{i,j} ((i-\mu) + (j-\mu))^4 g(i,j)$   |
| Haralick's Correlation    | $f_8 = \frac{\sum_{i,j} (i,j)g(i,j) - \mu_i^2}{\sigma_i^2}$   |

| Variable | Equation   |
|----------|--|
| $\mu$    | $\mu = \sum_{i,j} i \cdot g(i,j) = \sum_{i,j} j \cdot g(i,j)$                    |
| $\sigma$ | $\sigma = \sum_{i,j} (i-\mu)^2 \cdot g(i,j) = \sum_{i,j} (j-\mu)^2 \cdot g(i,j)$ |

(GLRLM) computed for each voxel's neighborhood. GLCM is a 2-dimensional histogram where

each axis represents all possible voxel values in a neighborhood. For a given pattern, each bin in the histogram records the number of instances in a neighborhood where two voxels of the specific value are arranged as the pattern specified. GLRLM is also a 2-dimensional histogram, the x axis represents all possible voxel values, while the y axis represents the number of consecutive occurrences of the same voxel value in a given direction. For a given direction, each bin in the histogram records the number of instances where a specific number of continuous voxels of a specific value are lined up in the specified direction. See Fig. 21 for illustration of the texture features.

Table 3 lists the features generated from GLCM and Table 4 for GLRLM features and their equations, in which  $g(i,j)$  is the element in the corresponding cell in the matrix  $g$ ,  $\mu$  is the weighted pixel average, and  $\sigma$  is the weighted pixel variance.  $\mu_t$  and  $\sigma_t$  are mean and standard deviation of the row sums in the GLCM and GLRLM matrix. Refer to Fig. 12 for illustration of the texture features.

Multiple parameters could be specified for computing the texture features, including the number of intensity bins for both the GLCM and the GLRLM matrices, the maximum

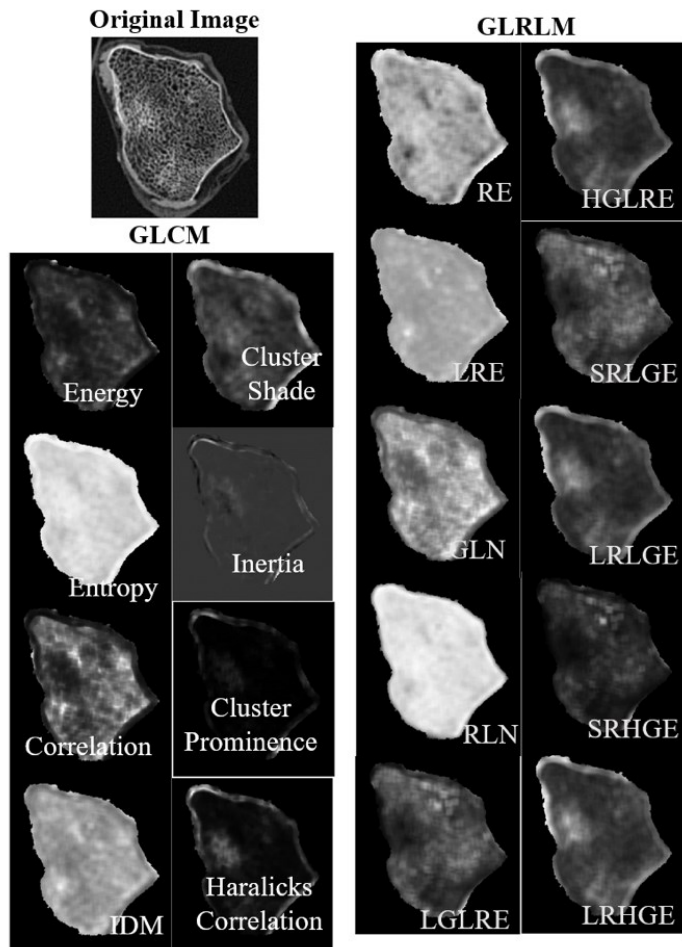
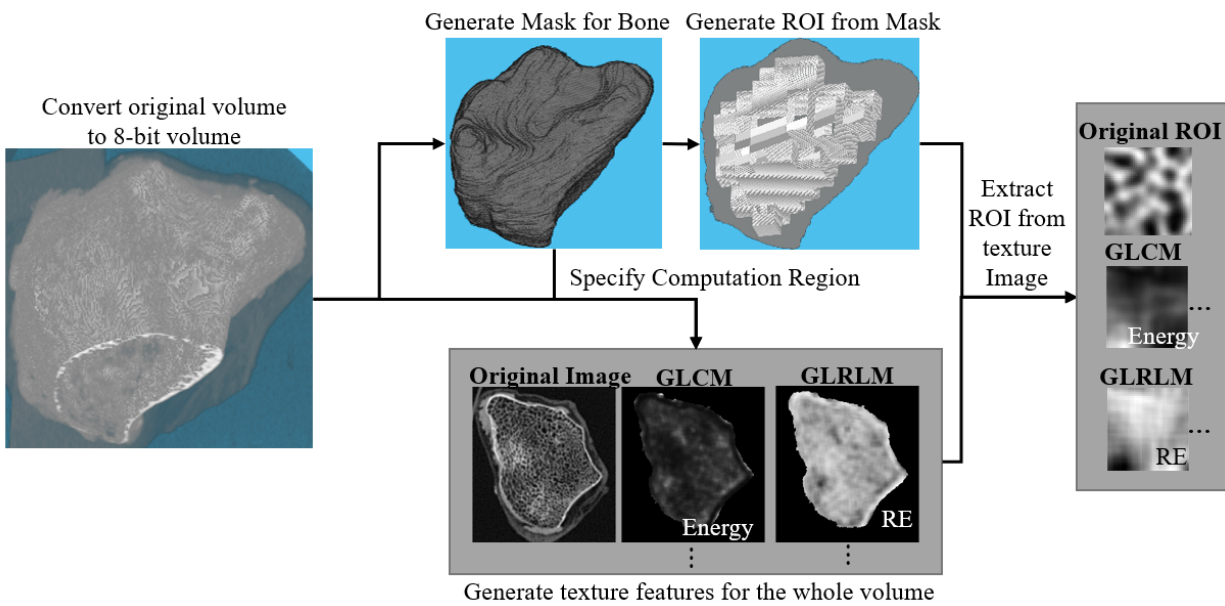


Figure 21: Illustration of GLCM and GLRLM texture features

radius of the neighborhood used to compute the texture matrix for each voxel, and the maximum run-length for computing the GLRLM. By default, the texture feature includes all possible intensity values, and the feature value is calculated as an average of the results from all possible pattern directions.

Texture features for each ROI were extracted as the mean value for all the voxels in the ROI (Refer to Fig. 22 for the texture generation pipeline).



**Figure 22:** Pipeline for generating the texture features

## 2.2.4 CBCT Reconstruction and Bone Mineral Density Analysis

Pairs of human knee scans obtained two weeks apart were used for the BMD reproducibility analysis. Artifacts such as noise and streaking due to scatter and beam hardening could make the attenuation values from CBCT inaccurate and inconsistent, potentially causing the derived BMD to be erroneous. Reducing such artifacts could make the BMD measurement more reproducible which in turn facilitates better diagnosis.

To minimize scatter and beam hardening artifacts, we used a previously established polyenergetic penalized likelihood (poly-PL) reconstruction incorporating an ideal mixture model of tissues and an accelerated Monte Carlo-based scatter correction, as proposed by Cao et al [28] based on Elbakri et al [29]. The Poisson maximum likelihood objective function for the reconstruction was formulated in terms of base materials: water and calcium carbonate [28]. The algorithm finds the densities of the two materials in each voxel [28].

An initial reconstruction was first obtained using FDK with a  $0.8 \times$  Nyquist frequency cutoff. Using the proposed ideal mixture model, the attenuation value of each voxel in the volume was interpolated into density. The density volume was subsequently used for a Monte

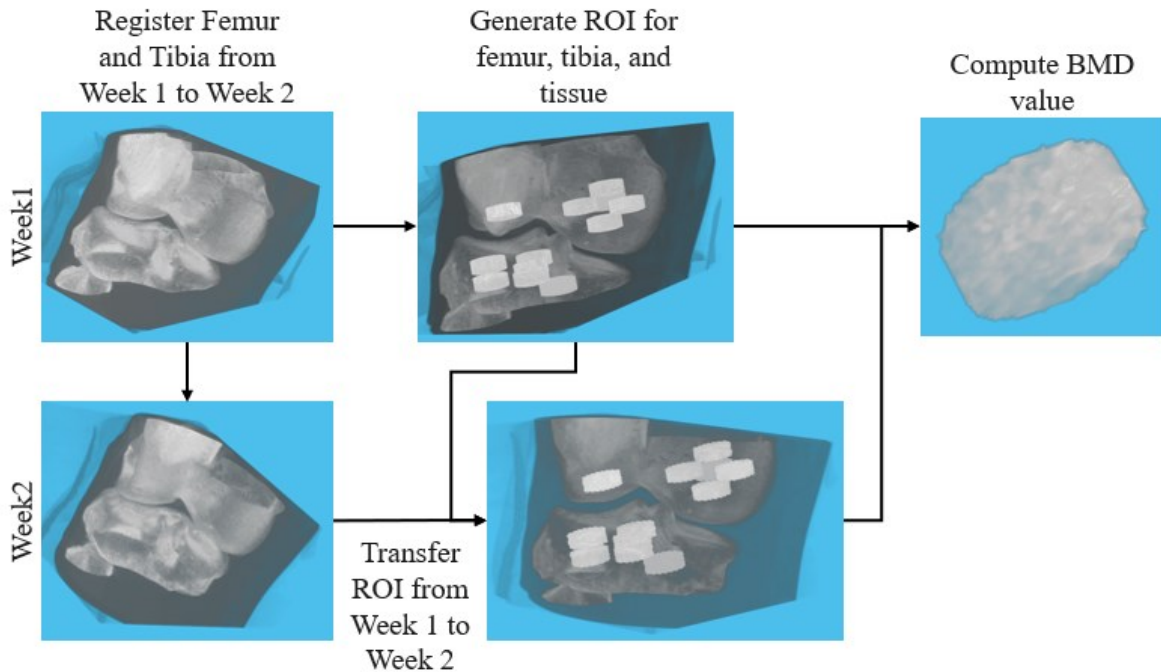


**Figure 23:** Illustration of the BMD analysis pipeline

Carlo-based scatter correction and for initialization of poly-PL (after 3 iterations of FDK and Monte Carlo scatter correction). The edge preserving Huber penalty was used as a regularization term in poly-PL. Optimization was terminated at 100 iterations. A FDK reconstruction with constant scatter correction was also generated along with the iterative reconstruction.

After reconstruction, the pairs of scans of the same subject – separated by a 2-week interval where we assumed no change in BMD – were registered using MITK. Tibia and Femur were registered separately to account for discrepancies in knee angle. ROIs were defined for Femur, Tibia, and tissue in the proximity of each bone in the first of the two scans. Those ROIs were transferred to the second scan using the registration transforms. Mean voxel value was computed for each ROI for further analysis.



# Chapter 3

## *Performance Evaluation of UHR-MDCT*

### 3.1 Sources of Data and Imaging Protocols

An ~18 cm plastic cylinder containing samples of a human radius, ulna, hamate, tibia plateau, and a vertebra was used as the imaging phantom. The phantom was first imaged without any additional attenuators (referred to as an In-Air scan) at different x-ray exposure levels (5 - 100 mAs). In a subset of the scans, the phantom was embedded in an anthropomorphic thorax phantom (QRM-Thorax, QRM GmbH) to study how the imaging dose and anatomical background affects the metrics of trabecular microarchitecture. The scans including this extra phantom) at different x-ray exposure levels (25 - 375 mAs) are denoted In-Body.

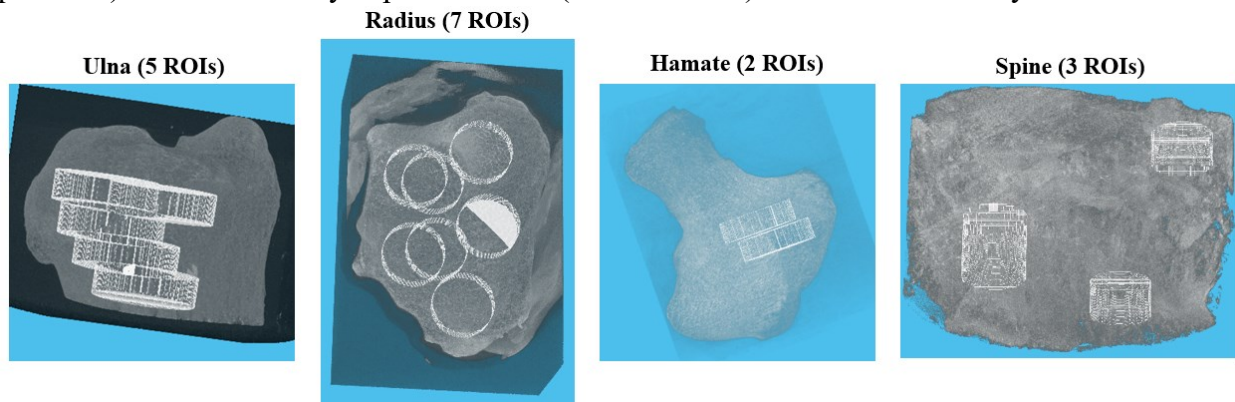


**Figure 24:** Illustration of the ROIs for UHR-MDCT performance analysis. Reconstructions were performed using Filtered Back Projection (FBP) with a variety of kernels including FC30, FC30 with iterative reconstruction, FC50, FC81, and FC81 with iterative reconstruction. Reference micro-CT volumes of each bone sample were obtained using a SkyScan 1172 system at 28 micron voxel size. For the analysis of the geometric morphometry of trabecular microarchitecture, both the UHR and NR MDCT volumes were resampled onto a



~0.028mm grid to match the voxel size of the micro-CT. We also studied how the reconstruction kernel and dose affect the robustness of radiomic texture features.

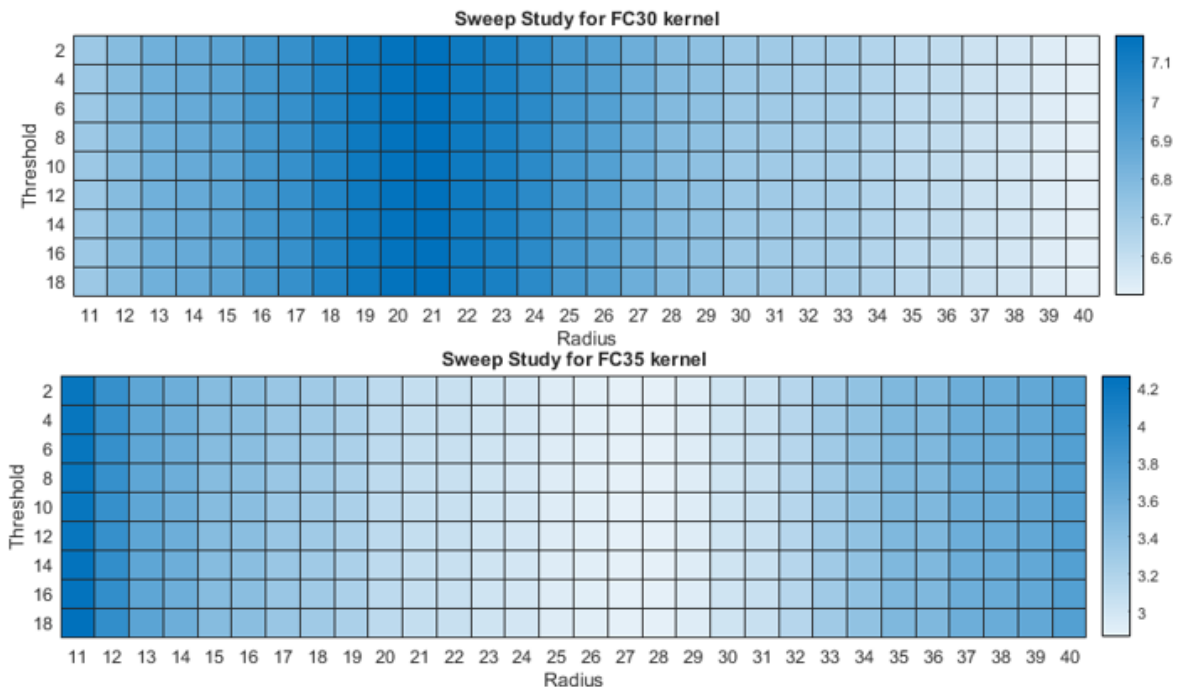
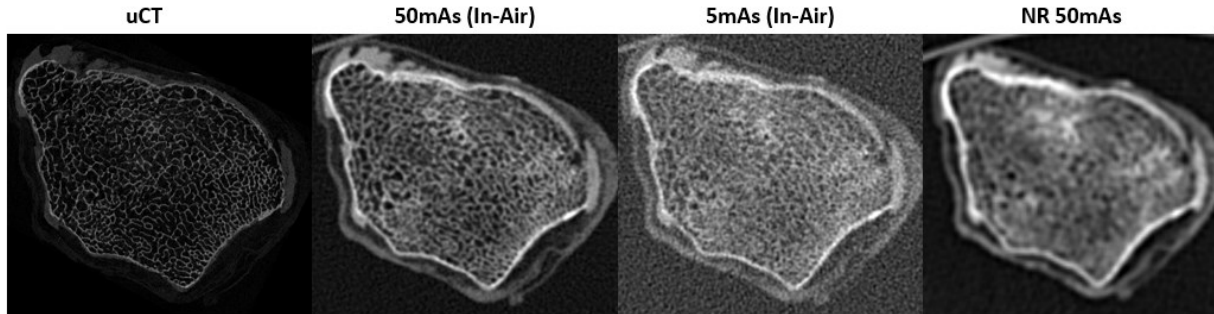


**Figure 25:** Heatmap for the sweep study of reconstruction kernels and segmentation parameters for UHR-

An initial parameter sweep was conducted to determine the sharpest reconstruction filter and Bernsen segmentation settings that yielded the best correlation with micro-CT. The phantom was scanned at 87 mAs and reconstructed with all reconstruction kernels. Cylindrical ROIs (diameter = 320 voxels and height = 90 voxels) were selected for each bone's micro-CT volumes (refer to Fig. 24) and registered to bone volumes from other modalities and imaging protocols using MITK. A range of radius and contrast thresholds was tested in the Bernsen's segmentation's parameter sweep. Trabecular metrics for the various reconstruction kernels and segmentation parameters of UHR-MDCT were generated (Refer to Fig. 25). It was determined that the FC30 reconstruction kernel, along with a radius of 20 voxels and threshold of 30 image intensity for the Bernsen segmentation resulted in the best overall correlation of UHR MDCT

with micro-CT in BvTv, Tb.Th, and Tb.Sp. Threshold = 20 image intensity and Radius = 15 voxels was determined to be the optimal setting for segmentation of NR MDCT.

### 3.2 Trabecular Morphometry



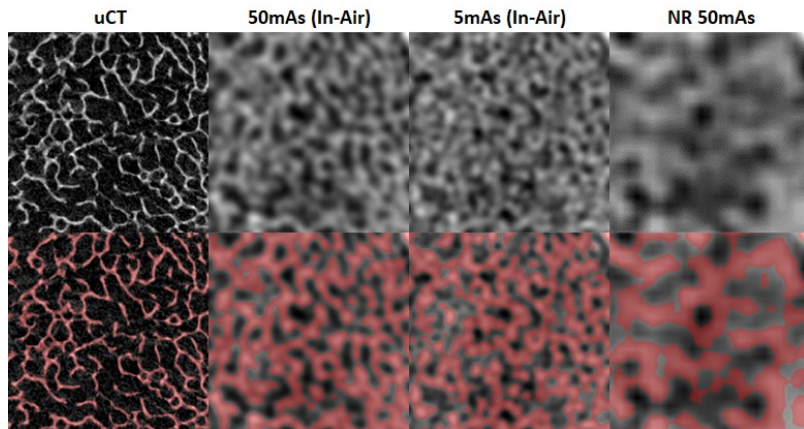
**Figure 26:** Images of a human radius obtained by micro-CT, 50mAs UHR-MDCT (In-Air), 5mAs UHR-MDCT (In-Air), and NR (50mAs)

Fig. 26 shows a comparison between UHR- and NR-MDCT for a human radius sample.

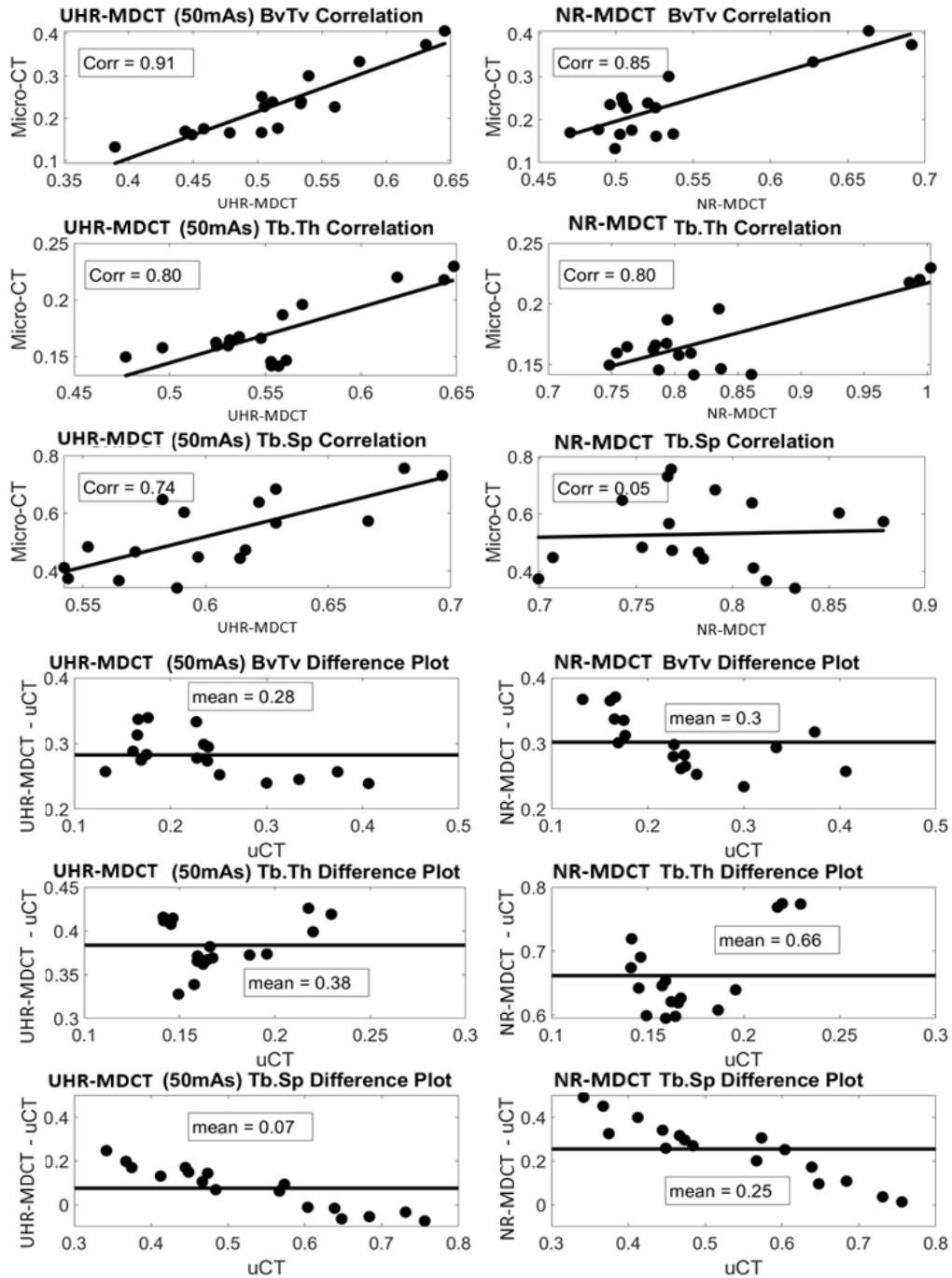
The gold standard micro-CT is also included for reference. It can be observed that even at 5mAs the UHR-MDCT is able to reveal more details of the fine trabecular structures than NR-MDCT, despite the significant increase in noise. Fig. 27 shows a matching ROI and its segmentation for each modality. It can be seen that both of the UHR-MDCT segmentations show better agreement with micro-CT than NR-MDCT.

Fig. 28 studies the correlation of UHR-MDCT and NR-MDCT with micro-CT at the matching MDCT exposure of 50mAs. As mentioned earlier, each data point represents the mean value extracted from an ROI.

UHR-MDCT is able to achieve a substantially better correlation than NR-MDCT in BvTv (correlation is 0.91 for UHR-MDCT and 0.85 for NR-



**Figure 27:** Matching ROI and Segmentation for Micro-CT, 50mAs (In-Air), 5mAs (In-Air), and NR (50mAs)



**Figure 28:** Correlation and difference plots of UHR-MDCT and NR-MDCT against micro-CT (at 50mAs)

MDCT) and Tb.Sp (correlation is 0.74 in UHR-MDCT and 0.05 for NR-MDCT). Both modalities yielded adequate correlation for Tb.Th (0.8 for both). It is worth noting that for NR-MDCT, the datapoints with higher BvTv and Tb.Th might bias the correlation estimate, whereas

the data points with lower BvTv and Tb.Th values have a more random distribution. The high level of correlation with micro-CT achieved by UHR-CT indicates that it could potentially track the change in trabecular geometry with performance comparable to micro-CT.

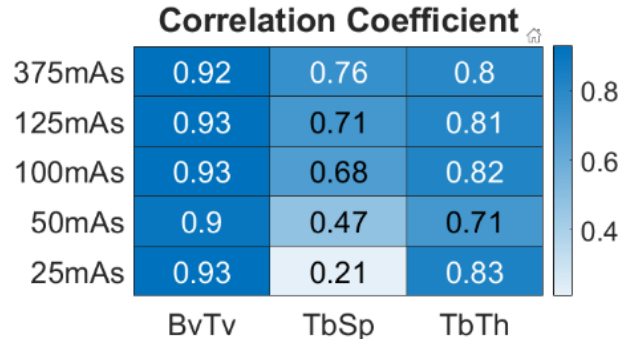


**Figure 29:** Correlation of FC30 In-Body scan at exposures ranging from 375mAs to 25mAs with Micro-CT

However, a high level of correlation with micro-CT does not imply a high level of quantitative agreement between the two modalities. Thus, the quantitative agreement between the two CT modalities and micro-CT metrics was also examined. Fig. 28 shows the difference between the measurements obtained with the CT modalities and micro-CT, plotted against the micro-CT value. The mean deviation was calculated as the average deviation across all ROIs. It can be seen from Fig. 28 that both UHR- and NR-CT show a significant deviation from the micro-CT measurements. However, measurements from UHR-MDCT generally have a smaller deviation than NR-CT, especially for Tb.Th and Tb.Sp (mean deviation of 0.25 for NR-MDCT compared to 0.07 for UHR-MDCT).

The effect of scan exposure on UHR-MDCT trabecular morphometric measurements was studied using In-Air scans. The correlation between scans at different exposure and micro-CT is presented in Fig. 29. Scan exposure had minimal effect on the three metrics down to 100mAs. Below 100mAs, the correlation of Tb.Sp was significantly reduced, indicating that image noise had a greater effect on the extraction of this trabecular metric. Fig. 30 shows the slice views of an FC30 In-Body scan at 375 mAs and 50 mAs.

### 3.3 Radiomic Texture Features of Bone

#### 3.3.1 Parameter Sweep

A parameter sweep was conducted for texture features, by varying the number of intensity bins, the maximum radius of the computation neighborhood, and the maximum run-length distance. The cylinder was embedded in the thorax phantom as described above and it was scanned at 375mAs. The same ROIs

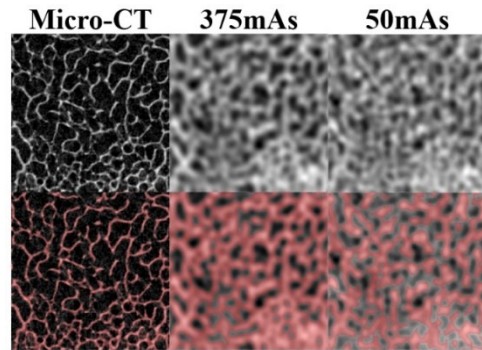


**Figure 30:** Illustration of FC30 In-Body scan at 375mAs and 50mAs

used in the trabecular morphometry study were used for the parameter sweep. The original volumes were converted to 8-bit. The range of values for the intensity bin number was varied from 60 to 100, while the range for the maximum neighborhood radius was varied from 4 to 10 voxels, and the range for the maximum run-length distance was varied from 4 to 16. Texture features were generated for all combinations of the parameters.

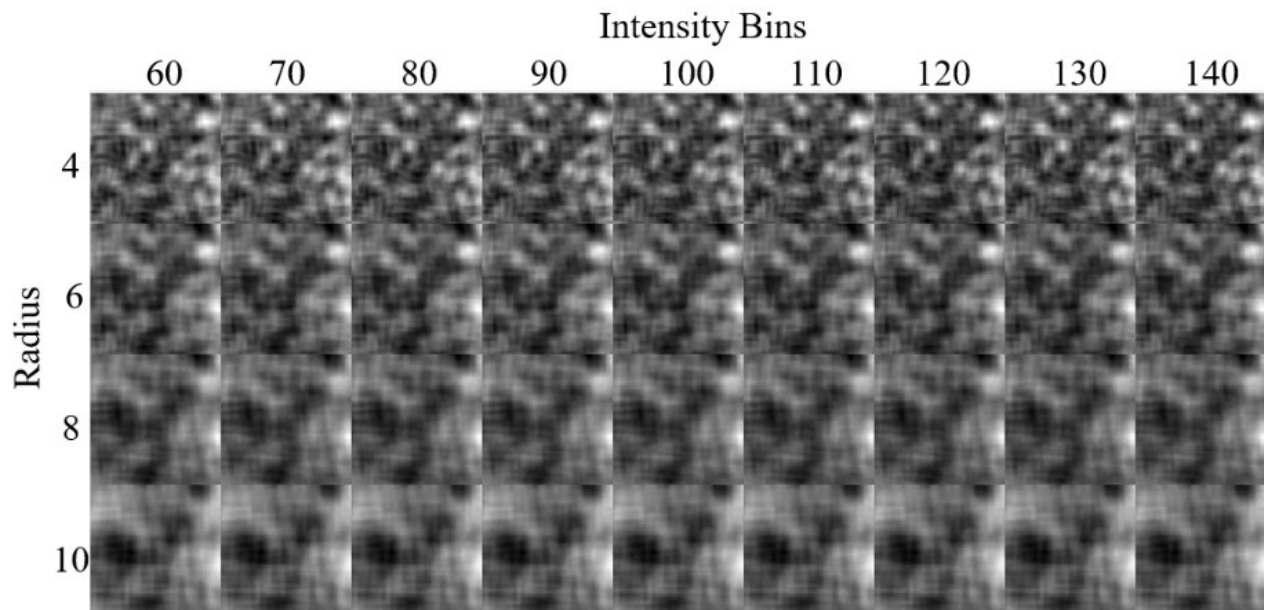


**Figure 31:** Example plot used for visual examination of texture features as a function of the parameters of the texture extraction algorithm (here for the feature of Inverse Difference Moment)



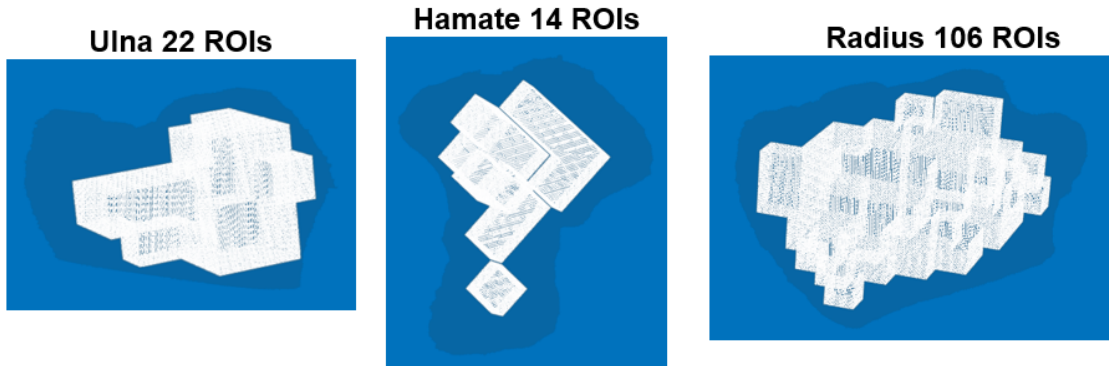


**Figure 32:** Illustration of the ROIs for Texture Feature analysis in UHR MDCT.

Optimal parameter values were determined through visual inspection and by analysis of correlation across different reconstruction settings. Specifically, we chose parameters that produced the highest correlation between the results across reconstruction settings, which indicated that the algorithm was able to extract similar trends from scans of the same bone under varying imaging protocols. Visual examination of the texture volumes was also conducted (Fig. 31). The final parameter set was 100 intensity bins, 8-voxel maximum run-length distance, and a neighborhood radius of 8 voxels.

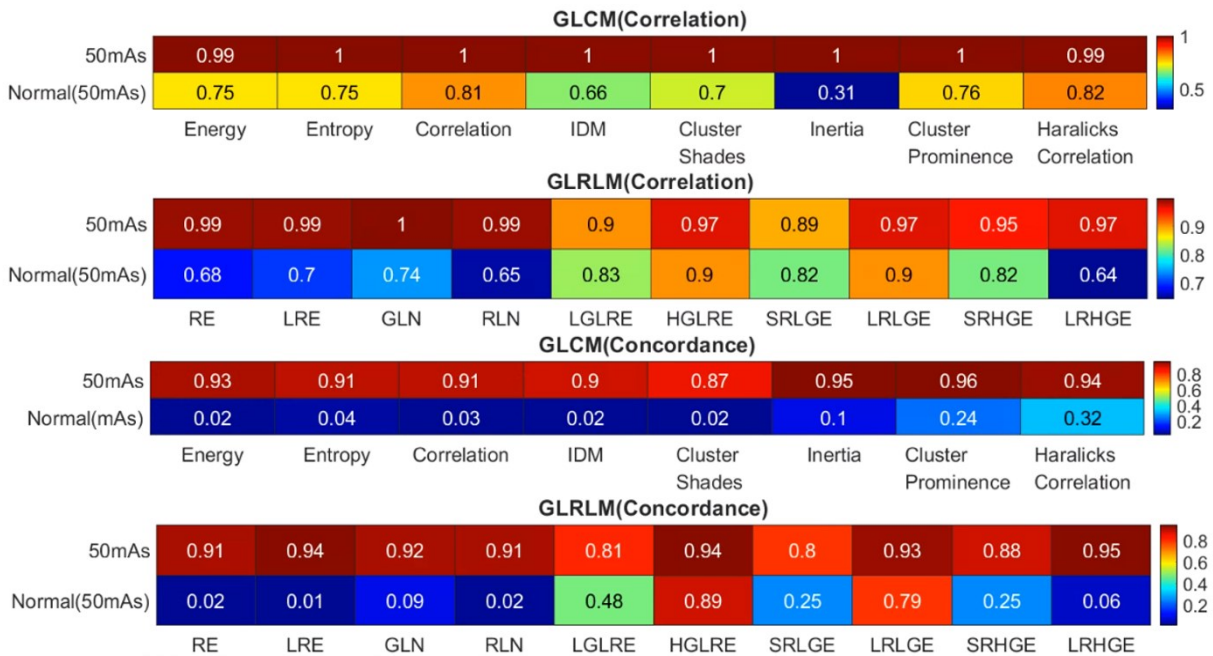


**Figure 33:** Heatmap illustrating the correlation between texture features (UHR-CT and NR-CT) at 50mAs and texture features of UHR-CT at 100mAs

### 3.3.2 Texture Features

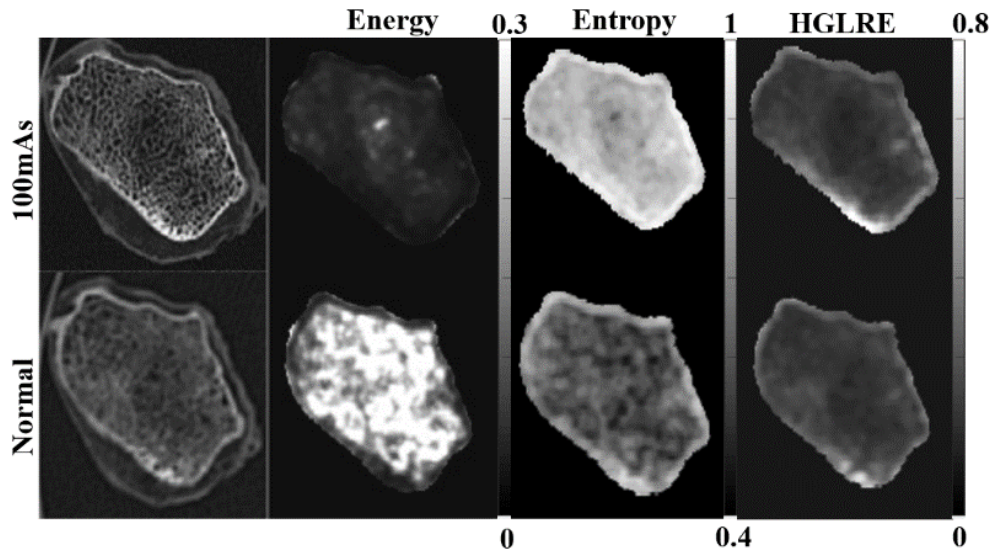


**Figure 34:** Illustration of GLCM and GLRLM features (Energy, Entropy, and HGLRE)

Due to the uneven presence of trabecular structures, the spine bone sample was excluded from the texture analysis. A new set of square ROIs with a side length of 40 voxels were generated for this analysis (Fig. 32). ROIs were cropped from the texture feature volume and each ROI measurement was obtained as the mean of texture features over all voxels.

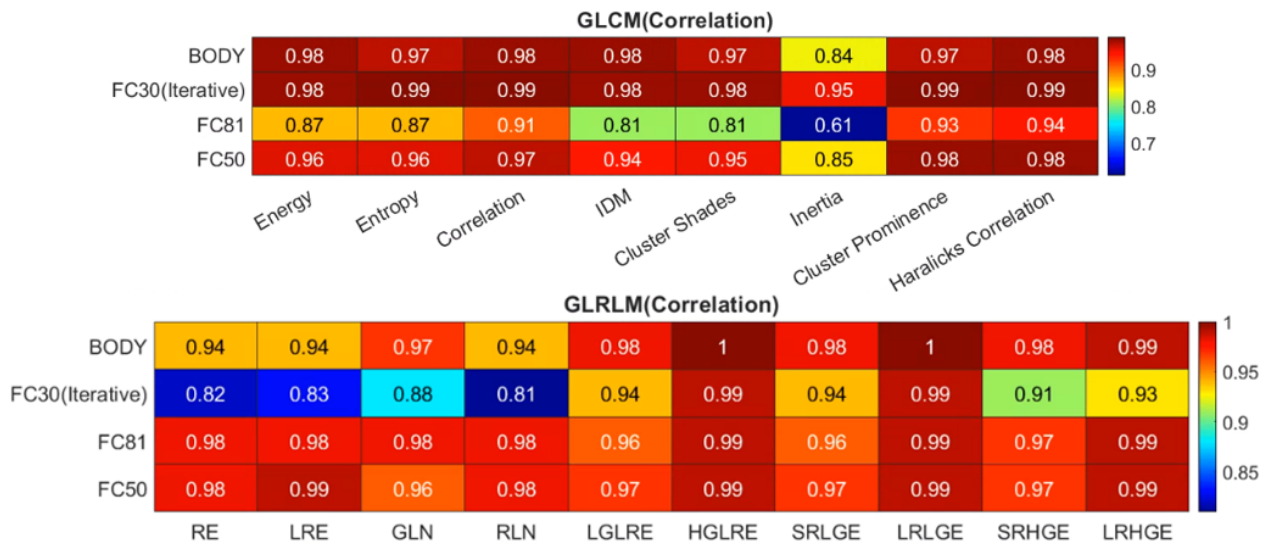


**Figure 35:** Correlation of texture feature between FC30 and other reconstruction kernels

GLCM and GLRLM texture features were examined for UHR-MDCT and NR-MDCT at 50mAs (Fig. 33). Both the correlation and concordance correlation coefficient (CCC) were investigated against UHR-CT at 100mAs. For UHR-CT at 50mAs, all texture features were able to achieve a high level of correlation (greater than 0.8); the majority achieved correlations greater than ~0.9. Therefore, for UHR-MDCT, the texture features appear mostly insensitive to confounding factors such as noise. For NR-MDCT, the correlations with 100mAs UHR-MDCT are generally high (correlation and Haralicks correlation from GLCM features >0.8, and HGLRE and LRLGE from GLRLM features >0.9). However, the CCC for NR-MDCT against UHR-MDCT was generally poor. For GLCM, Energy, Entropy, Correlation, IDM, and Cluster Shades,

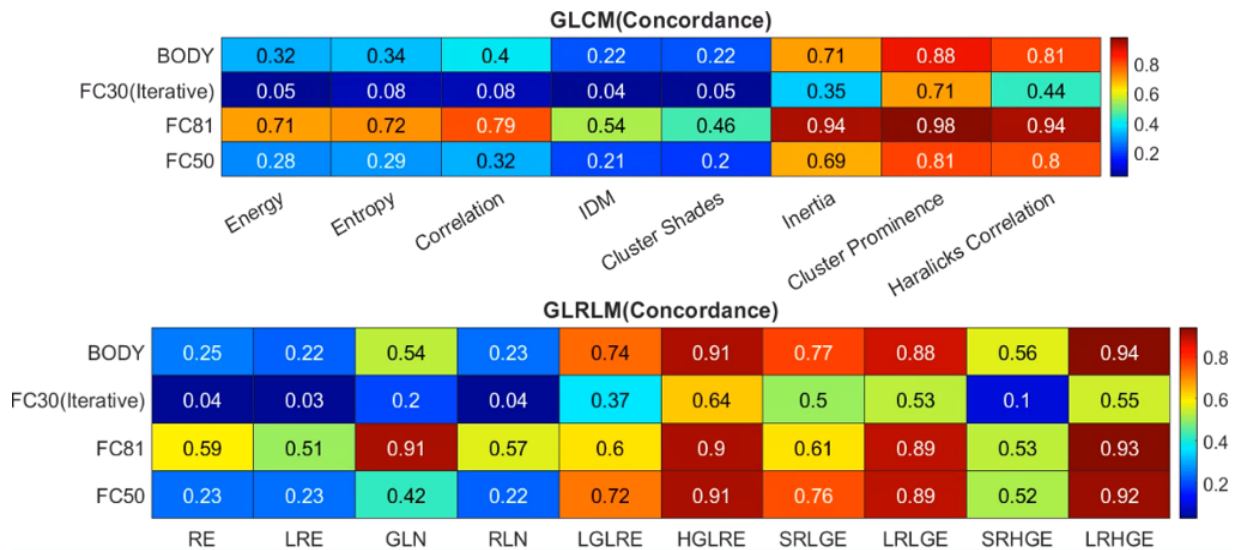


**Figure 36:** Concordance Correlation Coefficient of texture features between FC30 and other reconstruction kernels.

CCC was generally around 0.05. For GLRLM, the CCC of most features were also around 0.05. However, features with emphasis on either high or low gray levels generally produced a higher CCC, and features with long run emphasis achieve concordance comparable to that of UHR-CT (HGLRE and LRLGE with concordance~0.8). Since CCC takes into account the quantitative agreement of two variables in addition correlation, it does indicate a poor reproducibility of the absolute magnitude of the texture features between UHR and NR-MDCT. However, the high



correlation of the texture features might be sufficient to enable the application of previously developed NR-MDCT-based predictive algorithms using texture analysis to UHR-MDCT.

The reproducibility of UHR-MDCT texture features across reconstruction algorithms was also investigated. The same ROIs were used for this analysis. UHR scans at 375mAs were used for the study. Four reconstruction kernels were investigated: FC30 using iterative reconstruction, BODY (deep learning based reconstruction), FC81, and FC50. Fig. 35 provides a summary of the results. All four reconstruction kernels were able to achieve high levels of correlation against FC30 UHR-MDCT (all correlations higher than or equal to 0.8 except Inertia in the deep learning-based reconstruction). For CCC, shown in Fig. 36, all reconstruction kernels (except for FC81) exhibit poor reproducibility in some of the texture features. Features such as energy, entropy, correlation, IDM, and Cluster Shades in GLCM, and RE, LRE, and RLN in GLRLM show a consistently low correlation (0.2-0.3) for all kernels beside FC81, which was able to achieve an adequate correlation for all of the texture features. The result indicate that the UHR-MDCT reconstruction kernels affect the absolute values of the texture features, but not necessarily the trends in those features.

## Chapter 4

### *Performance Evaluation of CMOS-CBCT and FPD-CBCT*

#### 4.1 Sources of Data, Imaging Protocols (including Patient Study)

A set of 26 bone cores ~8mm in diameter extracted from 4 human cadaveric tibias was obtained through a collaboration with Hospital for Special Surgery (HSS, New York NY). The cores were used for the evaluation of the CBCT systems. A water cylinder (~50mm diameter) containing BMD calibration inserts (75mg/mL CaHa and 150mg/mL CaHa) was placed in the same field of view as the bone cores (see Fig. 37 for the scan setup). This setup was imaged using a conventional MDCT, the aSi FPD-CBCT, and the CMOS-CBCT. Each core was individually imaged on a micro-CT system as the gold standard. The CBCT performance in trabecular morphometric measurement structures were studied in this dataset together with its ability to measure the statistics of Rod-like and Plate-like trabeculae. Metrics from CBCT were compared to metrics obtained with micro-CT. Due to low trabecular mineral content, one sample set (8 cores) was removed from the analysis.

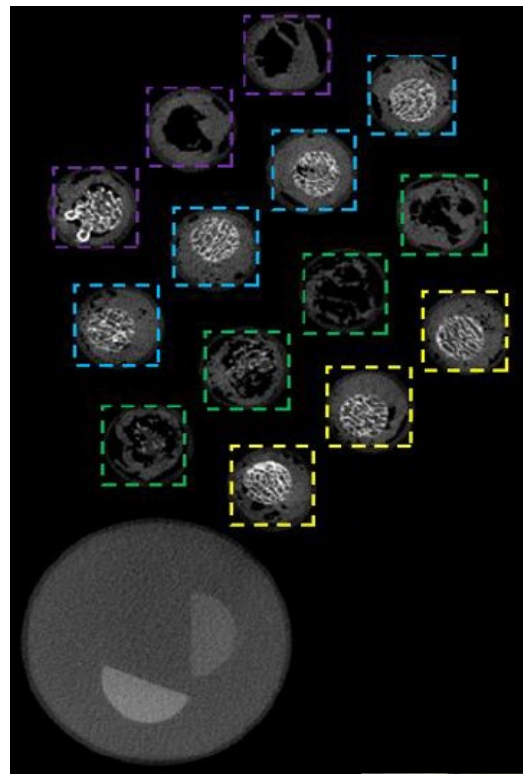


**Figure 37:** Axial slice showing the configuration of the 26 bone samples extracted from 4 cadaveric tibias used in the performance evaluation of CBCT (with BMD inserts)

Human subject data (Fig. 38) was used to study the reproducibility of BMD measurements from the CBCT system as described in Sec. 2.2.4.

## 4.2 Trabecular Morphometry

After reconstruction and rescaling to BMD, the individual bone cores were segmented individually. For each micro-CT bone core volume, a mask that excludes the outer shell trabecular structure was generated. As mentioned in the Methods section, the bone masks were then transferred to a corresponding position in the CBCT and MDCT images using a transformation obtained through image registration.

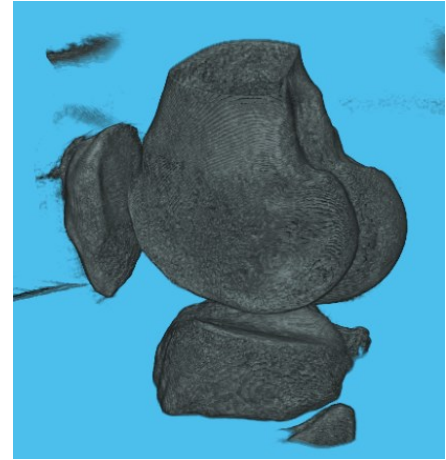


Figure 38: Example patient knee scan for BMD reproducibility analysis

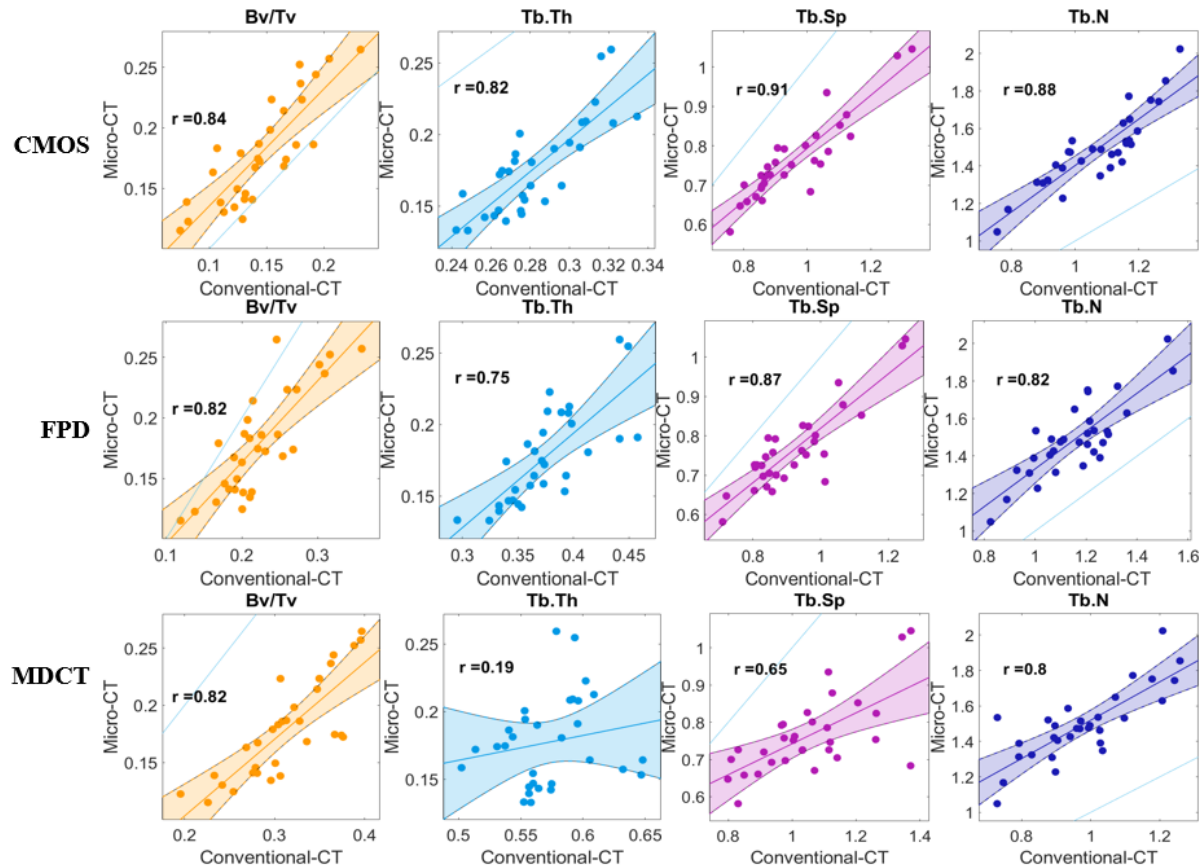
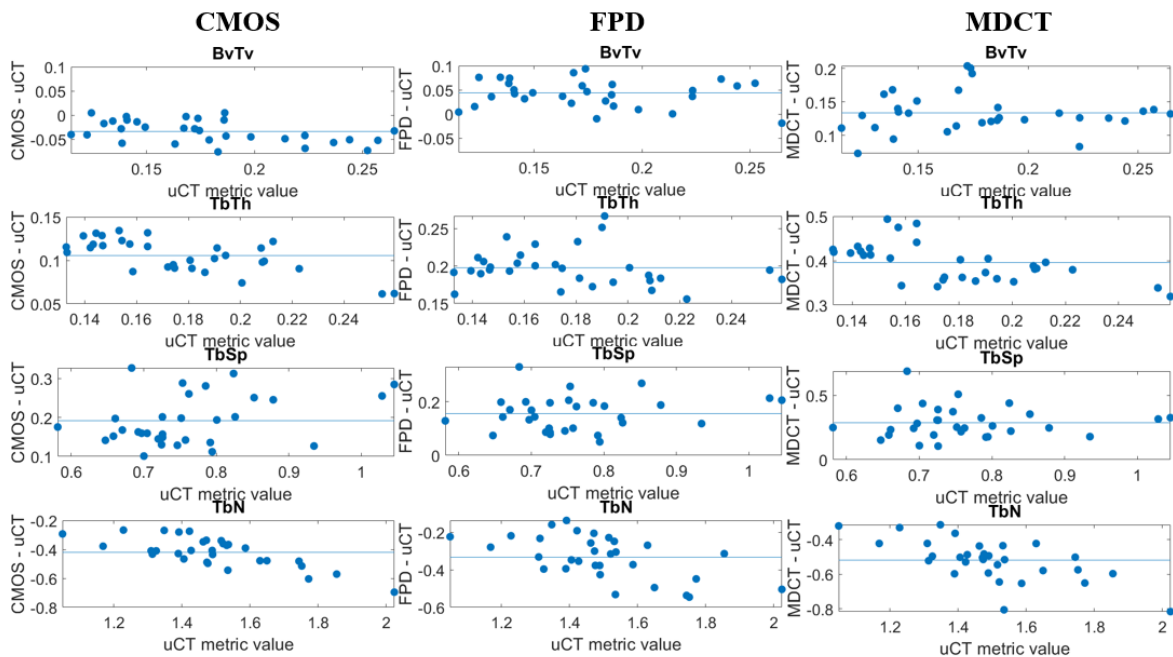


Figure 39: Trabecular metrics for aSi FPD-CBCT, CMOS-CBCT, and MDCT

Due to the high noise and the presence of soft tissue and drilling debris in the trabecular cavities, a high global pre-thresholding at BMD value of 70 was applied to each bone core prior to Bernsen’s segmentation. Previous studies indicated that thresholding at 70 BMD helps in removing the majority of confounding background structures.

A parameter sweep was carried out to determine the optimal neighborhood radius (range 4-15 voxels) and contrast threshold (range 2-202 image intensity) for Bernsen’s segmentation. Due to the difference in voxel size (CMOS and FPD-CBCT have a 100  $\mu\text{m}$  voxel size, MDCT have a  $\sim 250 \mu\text{m}$  voxel size), two set of parameters were established, one for aSi FPD- and CMOS-CBCT and one for MDCT. We chose segmentation settings that produced adequate



**Figure 40:** Difference plots (Bland-Altman-type) between the three modalities (CMOS-CBCT, aSi FPD-CBCT, and MDCT) and micro-CT plotted against the micro-CT metric value.

correlations against the ground truth in the initial sweep, with balanced performance across all four metrics: a radius of 9 voxels and threshold of 42 image intensity for aSi FPD- and CMOS-CBCT, and a radius of 2 voxels and threshold of 2 image intensity for MDCT. Otsu segmentation was used for binarization of the micro-CT volumes.

Trabecular metrics were generated using the pipeline described in the Methods section. The metrics for the three modalities were analyzed by comparison with gold standard micro-CT measurement. For BvTv and Tb.N, all three modalities achieved good correlation with micro-CT (~0.8 or higher). For Tb.Th and Tb.Sp, a significant improvement in correlation can be observed in CBCT compared to MDCT. Although little improvement in terms of correlation was observed in BvTv, the least square best fit line is more aligned with the identity line, suggesting the BvTv could potentially be measured with more quantitative accuracy. Different from BvTv, which counts the total number of voxels in an ROI, metrics such as Tb.Th and Tb.Sp convey structural information. The significantly higher correlation of Tb.Th and Tb.Sp suggests that change in trabecular structure can be tracked with more sensitivity using CBCT, in particular CMOS-CBCT. Bland-Altman-type difference plots for the three modalities against micro-CT are shown in Fig. 40. It could be observed that, although the difference in the measured magnitude of the

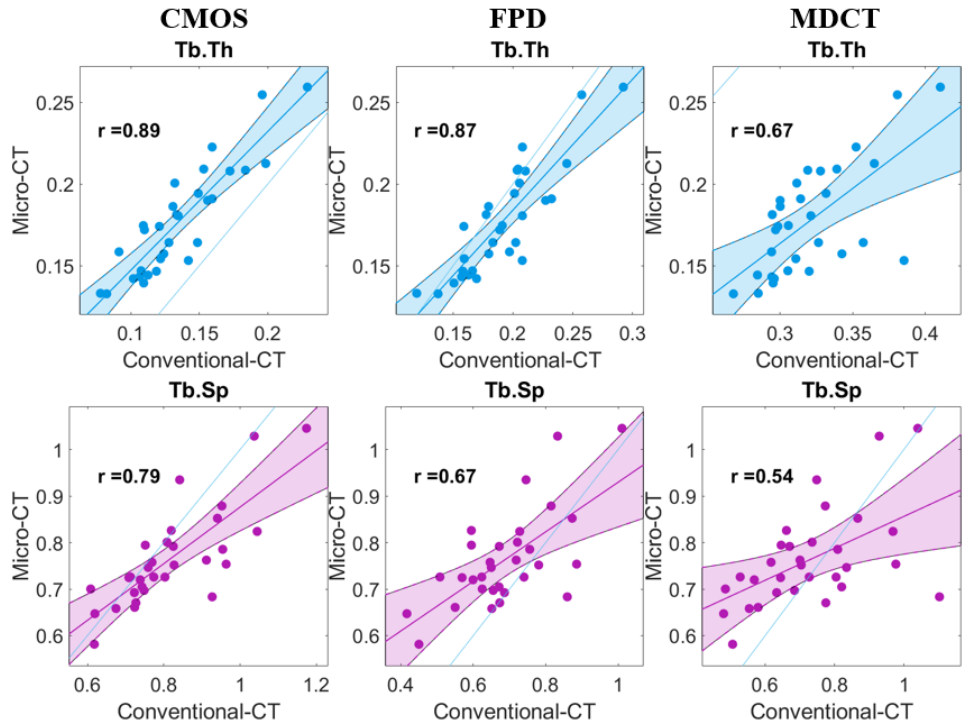


**Figure 41:** Correlations of derived metrics (Tb.Th and Tb.Sp) for CMOS-CBCT, aSi FPD-CBCT, and MDCT

three metrics between the clinical modalities and micro-CT remains substantial, there is a

significant reduction in metric difference for the CBCT modalities compared to MDCT. Overall, CMOS-CBCT improves the correlations with micro-CT compared to aSi FPD-CBCT and MDCT, as anticipated based on its high spatial resolution. Therefore, CMOS-CBCT might provide a more sensitive tool to track changes in bone microstructure compared to the existing modalities. At the same time, achieving accurate measurements of microstructural metrics such as Tb.Th (as opposed to detecting trends in those structural features) remains a challenge using clinical imaging technologies, although the new high-resolution modalities yield a clear improvement in this respect as well.

#### 4.2.1 Derived Trabecular Metrics

The studies in the previous subsection utilized direct measurements of Tb.Th and Tb.Sp obtained from CBCT and MDCT volumes. An alternative approach, previously developed for lower resolution imaging technologies, involves deriving those metrics from BvTv and TbN, which are less sensitive to system resolution [30].

$$Tb.Th(\text{derived}) = BvTv/TbN$$

$$Tb.Sp(\text{derived}) = (1 - BvTv)/TbN$$

The derived Tb.Th and Tb.Sp metrics were also computed for CBCT and MDCT and compared to the gold standard micro-CT measurement. As shown in Fig. 41, the derived Tb.Th metric exhibits overall a better correlation with micro-CT than the directly measured metric does; a significant improvement in correlation can be observed for MDCT (from 0.19 to 0.67). However, an overall decrease in correlation is observed for Tb.Sp in all modalities, revealing the complex tradeoffs between the settings of the segmentation algorithm and the technique used to obtain the trabecular measurements (note that the segmentation settings were not optimized for

derived metrics – rather, we used the same settings as in the direct measurements of the previous section).

### 4.3 Rods and Plate

#### Morphology

We used digital topological analysis to classify the trabeculae into rods and plates in CMOS-CBCT, aSi FPD-CBCT, and micro-CT

(reference gold standard). The skeletonization was visually inspected at different cross sections of the volumes (Figs. 42 and 43). Rod to Plate ratio was computed for each bone core scanned with FPD-CBCT, CMOS-CBCT, and Micro-CT. CBCT performance was analyzed against the gold standard micro-CT result.

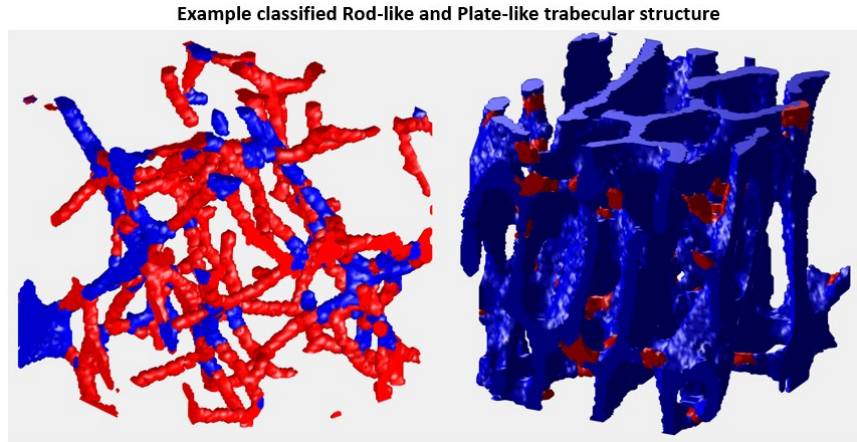


Figure 42: Illustration of the classification of rod-like and plate-like trabecular



Figure 43: Visual Inspection of the thinning algorithm

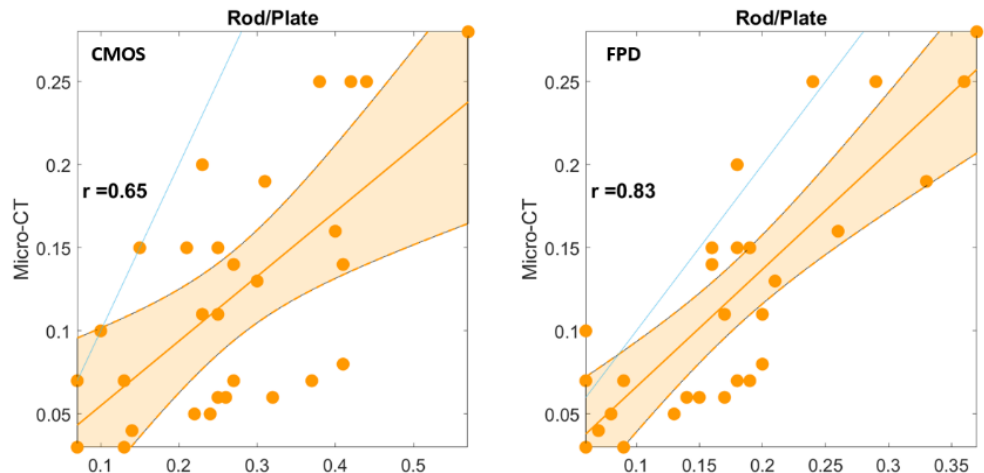
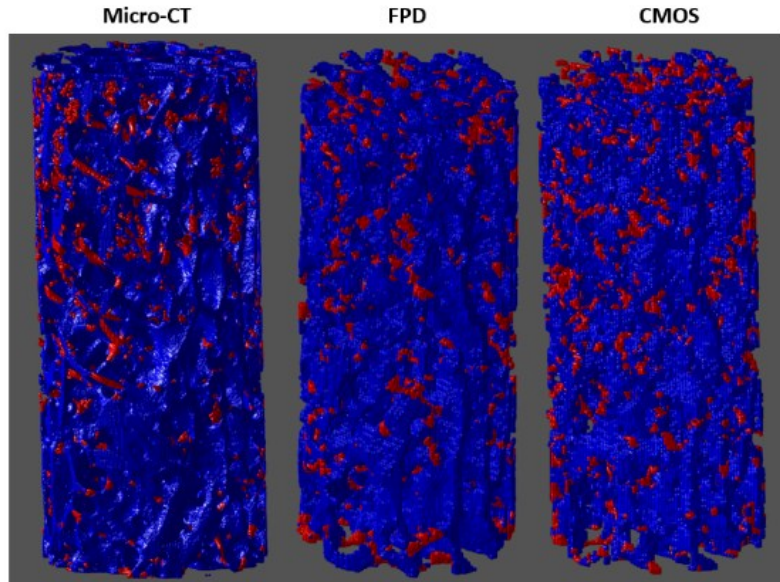


Figure 44: Correlation of CMOS and FPD Rod to Plate ratio against Micro-CT Rod to Plate ratio



Results lead to the conclusion that the topological analysis is resolution dependent. Thus, a parameter sweep study was conducted to determine the level of up-sampling of the binarized CBCT volume needed before the topological analysis.  $3\times$  up-sampling was determined



**Figure 45:** Classification result from Micro-CT, FPD, and CMOS

to be optimal as it produced the highest correlation of the rod-plate ratio with micro-CT.

Fig. 44 studies CBCT performance in quantifying rod to plate ratio in the trabecular region. It could be observed that aSi FPD-CBCT, achieves better correlation with micro-CT than CMOS-CBCT, despite its lower spatial resolution. This might be because the smoother appearance of aSi FPD-CBCT volumes is better suited for the skeletonization algorithm than the sharper, but slightly noisier CMOS-CBCT images (Fig. 45). Future work will involve optimization of CMOS-CBCT reconstruction protocols to improve the performance of the rod-plate analysis.

#### **4.4 BMD Reproducibility in CMOS-CBCT**

As described in the Methods section, the human subject data was used to assess the reproducibility of BMD measurements obtained on CMOS-CBCT. This study investigates whether the beam hardening and scatter corrections developed for CMOS-CBCT are sufficient to enable robust BMD evaluation.



A total of 12 ROIs with a radius of 15 voxels and 10 voxels thickness were generated for each bone scan, 5 for the femur, 5 for the tibia, and 2 for tissue in the proximity of each bone (see Fig. 46 for ROI illustrations). As explained earlier, the ROIs were first generated in the FDK patient scans from the first week and then transferred by registration to the second week data and to the Poly-PL reconstructions.

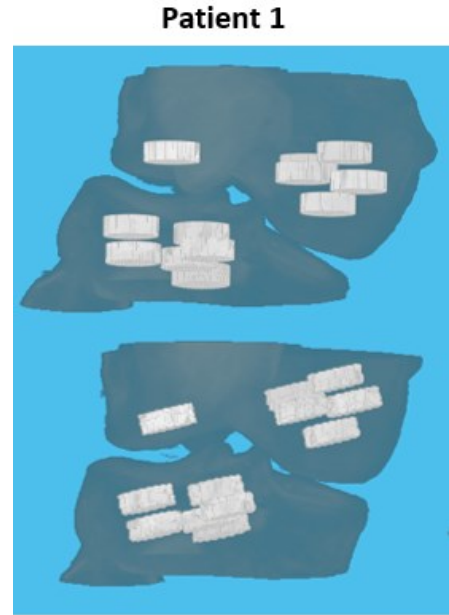


**Figure 46:** Illustration of ROIs for BMD reproducibility analysis in human subjects CMOS-CBCT.

Corresponding ROIs of the same subject were compared between the two visits to study the reproducibility of the CMOS-CBCT system. Box plots of all the pixels

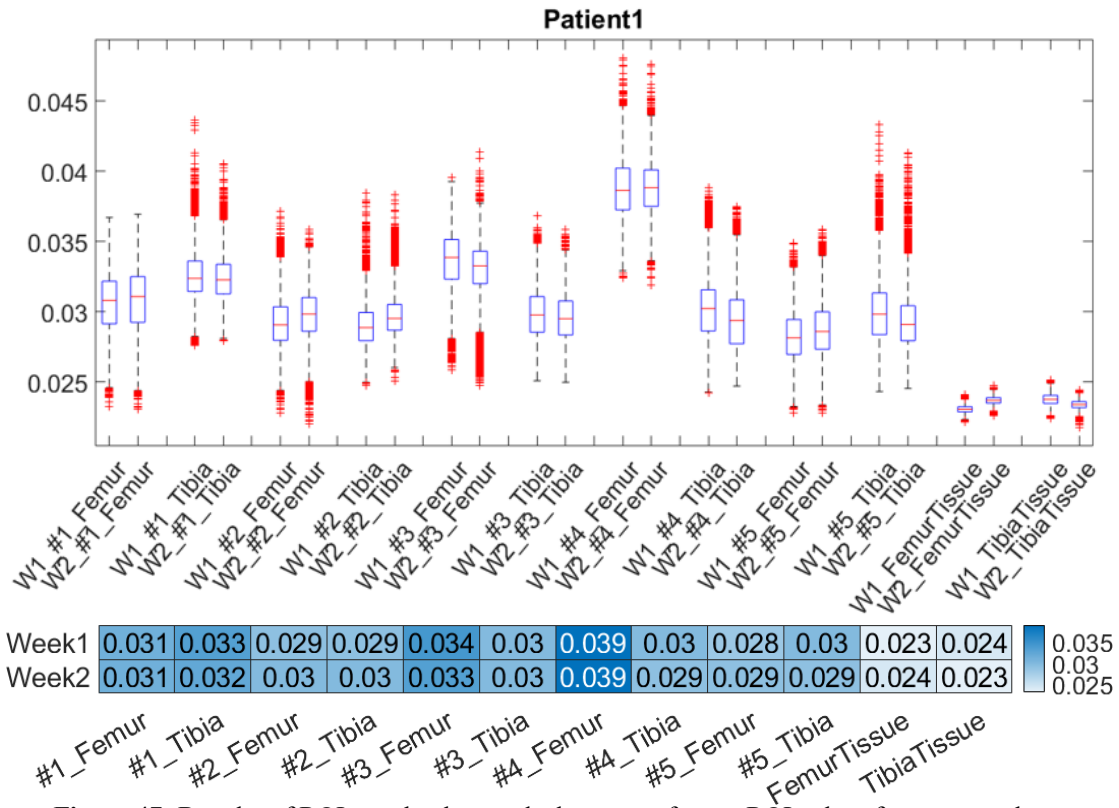


**Figure 47:** Boxplot of ROI voxel values and a heatmap of mean ROI values for an example human subject dataset.

within each ROI and heatmap of the mean ROI values were generated for this analysis (see Fig.

47 for an example box plot and heatmap for one of the subjects). Overall, the corresponding ROIs for the 8 patients had a similar mean value and distribution for both FDK and Poly-PL.

A paired t-test with 5% confidence interval was also conducted per patient if the ROI measurements from the two visits have the same mean and an overall difference of zero. For FDK, the t-test confirmed the hypothesis in 7 subjects and rejected the hypothesis in 1 subject. For Poly-PL, the t-test resulted in 6 accepts and 2 rejects. In general, the BMD measurements between the two visits were consistent with equal mean. The higher t-test rejection rate in Poly-PL could be due to the inaccuracy in ROI placement since a manual cropping step was involved in the Poly-PL volume processing. The high consistency of measurement across the two weeks suggests that the CMOS-CBCT with appropriate artifact corrections is capable of measuring BMD with good reproducibility.

# Chapter 5

## *Future Directions: Pixelated Scintillators*

The newly developed pixelated scintillator provides improved resolution compared to conventional unpixelated detectors of the same thickness. Fig. 48 shows a human ulna sample imaged using a gold standard micro-CT, a pixelated scintillator-based benchtop CBCT, and a

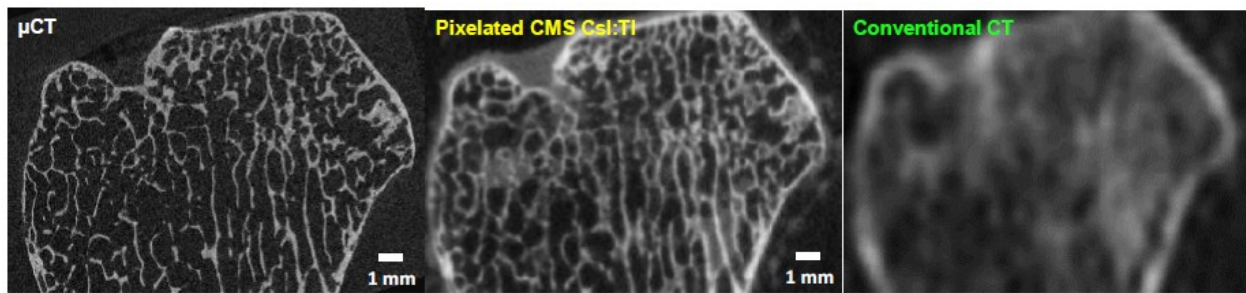


**Figure 48:** A scan of a human ulna obtained using Pixelated CMOS CSI:TI and conventional CT [2] conventional CT. The pixelated scintillator is able to reveal significantly more trabecular

structure than conventional CT. Fig. 49 shows a visual comparison of 2 trabecular ROIs

between micro-CT and a pixelated scintillator-based benchtop CBCT. The pixelated scintillator's

performance is also

evaluated in quantitative trabecular measurements.

High correlations against micro-CT are achieved by the pixelated scintillator:

~0.9 for BvTv, ~0.76 for Tb.Th, and ~0.82 for Tb.Sp.

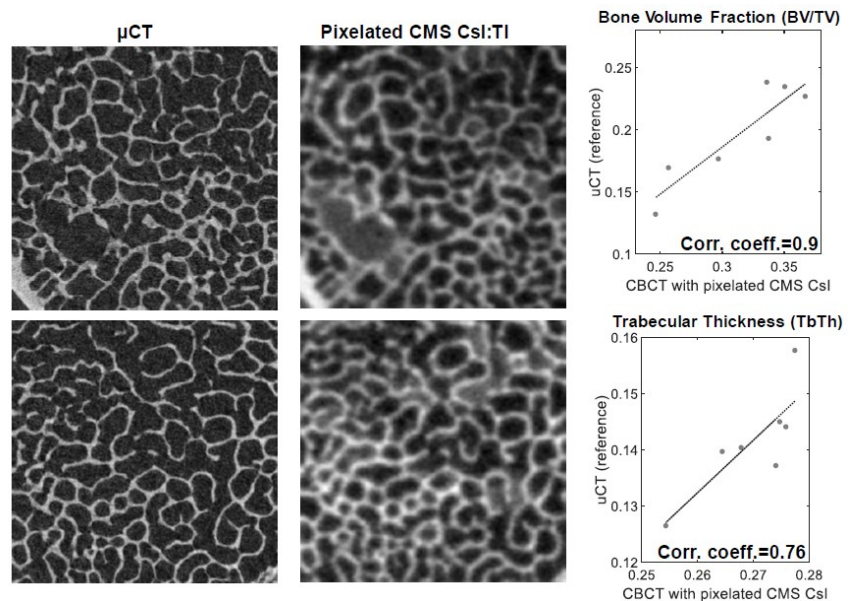


**Figure 49:** ROI comparison of Micro-CT and CMS CsI:TI with BvTv and TbTh correlation [2]

# Chapter 6

## *Discussion*

High-resolution extremity CBCT and UHR-MDCT demonstrate favorable performance in a range of bone biomarkers compared to the orthopedic imaging modalities in standard of care. UHR-MDCT was shown to be able to track the change in trabecular structure with high correlation against gold-standard micro-CT (over  $\sim 0.9$  for BvTv, over  $\sim 0.8$  for Tb.Th, and over  $\sim 0.7$  for Tb.Sp). A significant improvement from conventional CT was also observed in the accuracy of quantitative trabecular measurement. Texture analysis in UHR MDCT were observed to correlate well across changes in imaging dose and reconstruction kernel, as well as between NR-MDCT and UHR-MDCT. However, a change in system resolution (from NR-MDCT to UHR-MDCT) and reconstruction kernel did affect the magnitude of the texture features and thus the concordance between the modalities. Future work is thus needed to translate the predictive algorithms based on NR-MDCR bone texture features to UHR-MDCT.

Both CMOS-CBCT and aSi FPD-CBCT were able to track the change in trabecular structure with high correlation against micro-CT ( $>0.8$ ) for metrics of TbTh, TbSp, TbN, and BvTv. CMOS-CBCT offered a general improvement over aSi FPD-CBCT. Both CBCT systems were also able to assess rod and plate morphology, with aSi FPD-CBCT achieving a 0.83 correlation with micro-CT. CMOS-CBCT also demonstrated a high level of reproducibility in BMD measurements after the application of an advanced artifact correction framework, as shown in test-retest human subject data obtained two-weeks apart.

The new CT technologies evaluated in this thesis open up the possibility for improved diagnosis and understanding of bone disease. Biomarkers such as trabecular morphometrics and plate to rod ratio, which have been mostly inaccessible to in vivo CT imaging, could potentially become available for routine clinical application using CMOS-CBCT and UHR-MDCT. This thesis provided a principled technical evaluation of those new high-resolution technologies to support such clinical translation.

## Reference

- [1] "Musculoskeletal conditions." World Health Organization; <https://www.who.int/news-room/fact-sheets/detail/musculoskeletal-conditions>
- [2] S.R. Miller, B. Singh, M. S. J. Marshall, C. Brown, N. Sheth, G. Shi, J. H. Siewerdsen, W. Zbijewski, and V. V. Nagarkar. "Pixelated Columnar CsI:Tl Scintillator for High Resolution Radiography and Cone-beam CT." *Proceedings of SPIE Medical Imaging 2020: Physics of Medical Imaging* (2020); 1131212 (2020) <https://doi.org/10.1117/12.2550196>
- [3] H. Weinans, M. Siebelt, R. Agricola, S. M. Botter, T. M. Piscoer, and J. H. Waarsing. "Pathophysiology of peri-articular bone changes in osteoarthritis." *Bone*. 2012 Aug;51(2):190-6. doi: 10.1016/j.bone.2012.02.002.
- [4] G Li, J Yin, J Gao, T S Cheng, N J Pavlos, C Zhang, M H Zheng. "Subchondral bone in osteoarthritis: insight into . 2013;15(6):223. doi: 10.1186/ar4405.
- [5] J. M. Hootman, C. G. Helmick, K. E. Barbour, K. A. Theis, and M. A. Boring. "Updated Projected Prevalence of Self-Reported Doctor-Diagnosed Arthritis and Arthritis-Attributable Activity Limitation Among US Adults, 2015-2040." *Arthritis Rheumatol*. 2016 Jul;68(7):1582-7. doi: 10.1002/art.39692.
- [6] D. Leader, S.A. Williams, J.R. Curtis, and R. Weiss. Osteoporosis-Related Fracture Events in the US. *Journal of Clinical Densitometry*. 21. 1. 10.1016/j.jocd.2018.05.027.
- [7] C. M. Bono, T. A. Einhorn. "Overview of osteoporosis: pathophysiology and determinants of bone strength." *European spine journal : official publication of the European Spine Society, the European Spinal Deformity Society, and the European Section of the Cervical Spine Research Society*. 12 Suppl 2. S90-6. 10.1007/s00586-003-0603-2.
- [8] J. L. Prince, J. M. Links. "Medical imaging signals and systems." Upper Saddle River, N.J: Pearson Prentice Hall.
- [9] C.E. Cann. "Quantitative CT for determination of bone mineral density: a review." *Radiology*. 1988 Feb;166(2):509-22. doi: 10.1148/radiology.166.2.3275985.
- [10] "Bone Mass Measurement: What the Numbers Mean," NIH; <https://www.bones.nih.gov/health-info/bone/bone-health/bone-mass-measure>.
- [11] E. Saeedi, A. Dezhkam, J. Beigi, S. Rastegar, Z. Yousefi, L.A. Mehdipour, H. Abdollahi, and K. Tanha. "Radiomic Feature Robustness and Reproducibility in Quantitative Bone Radiography: A Study on Radiologic Parameter Changes." *J Clin Densitom*. 2019 Apr-Jun;22(2):203-213. doi: 10.1016/j.jocd.2018.06.004.
- [12] G. Lee, H.Y. Lee, H. Park, M.L. Schiebler, E.J.R. van Beek, Y. Ohno, J.B. Seo, and A. Leung. "Radiomics and its emerging role in lung cancer research, imaging biomarkers and clinical management: State of the art." *Eur J Radiol*. 2017 Jan;86:297-307. doi: 10.1016/j.ejrad.2016.09.005.
- [13] J.F. Veenland, J. Grashuis, H. Weinans, M. Ding, and H. Vrooman. "Suitability of texture features to assess changes in trabecular bone architecture." *Pattern Recognition Letters*. 23. 395-403. 10.1016/S0167-8655(01)00172-6.
- [14] M. B. Nagarajan, W. A. Checefsky, A. Z. Abidin, H. Tsai, X. Wang, S. K. Hobbs, J. S. Bauer, T. Baum, and A. Wismüller. "Characterizing Trabecular Bone structure for Assessing Vertebral Fracture Risk on Volumetric Quantitative Computed

- Tomography.” Proceedings of SPIE--the International Society for Optical Engineering, 9417, 94171E. <https://doi.org/10.1117/12.2082059>
- [15] S.J. Ferguson, T. Steffen. “Biomechanics of the aging spine.” *Eur Spine J.* 2003 Oct;12 Suppl 2(Suppl 2):S97-S103. doi: 10.1007/s00586-003-0621-0.
- [16] S. Subramanian, "METHODS FOR QUANTITATIVE ANALYSIS OF IN-VIVO BONE MICROSTRUCTURE USING COMPUTED TOMOGRAPHY," JScholarship, 2019.
- [17] T.R. Hildebrand, P. Rügsegger. “A New Method for the Model-Independent Assessment of Thickness in Three-Dimensional Images.” *Journal of Microscopy*(2003). 185. 67 - 75. 10.1046/j.1365-2818.1997.1340694.x.
- [18] X.S. Liu, P. Sajda, P.K. Saha, F.W. Wehrli, G. Bevill, T.M. Keaveny, and X.E. Guo. “Complete volumetric decomposition of individual trabecular plates and rods and its morphological correlations with anisotropic elastic moduli in human trabecular bone.” *J Bone Miner Res.* 2008 Feb;23(2):223-35. doi: 10.1359/jbmr.071009.
- [19] J. Wang, B. Zhou, I. Parkinson, C. D. Thomas, J. G. Clement, N. Fazzalari, and X.E. Guo. “Trabecular Plate Loss and Deteriorating Elastic Modulus of Femoral Trabecular Bone in Intertrochanteric Hip Fractures.” *Bone research*(2013). 1(4), 346–354. <https://doi.org/10.4248/BR20130400>
- [20] G. Shi, S. Sbramanian, Q. Cao, S. Demehri, J. H. Siewerdsen, and W. Zbijewski. "Application of a Novel Ultra-High-Resolution Multi-detector CT in Quantitative Imaging of Trabecular Microstructure." *Proceedings of SPIE Medical Imaging 2020: Biomedical Applications in Molecular, Structural, and Functional Imaging (2020)*; 113171E (2020) <https://doi.org/10.1117/12.2552385>
- [21] T.R. Hildebrand, P. Rügsegger. “A New Method for the Model-Independent Assessment of Thickness in Three-Dimensional Images.” *Journal of Microscopy* (2003). 185. 67 - 75. 10.1046/j.1365-2818.1997.1340694.x.
- [22] Brehler, M., Cao, Q., Moseley, K. F., Osgood, G., Morris, C., Demehri, S., Yorkston, J., Siewerdsen, J. H., & Zbijewski, W. (2018). Robust Quantitative Assessment of Trabecular Microarchitecture in Extremity Cone-Beam CT Using Optimized Segmentation Algorithms. *Proceedings of SPIE--the International Society for Optical Engineering*, 10578, 105781J. <https://doi.org/10.1117/12.2293346>
- [23] J. Bernsen. “Dynamic thresholding of gray-level images.” *Proc. of the 8<sup>th</sup> Int. Conf. On Pattern Recognition* (1986).
- [24] P. K. Saha, B. B. Chaudhuri, and D. D. Majumder, "A new shape preserving parallel thinning algorithm for 3D digital images," *Pattern Recognition*, vol. 30, pp. 1939-1955, 1997.
- [25] P. K. Saha and B. B. Chaudhuri, "3D digital topology under binary transformation with applications," *Computer vision and image understanding*, vol. 63, pp. 418-429, 1996.
- [26] J. Wang, B. Zhou, I. Parkinson, C. David, L. Thomas, J. G. Clement, N. Fazzalari, and X. E. Guo, "Trabecular Plate Loss and Deteriorating Elastic Modulus of Femoral Trabecular Bone in Intertrochanteric Hip Fractures," *Bone Research*(2013), vol. 1, p. 346–354. doi: 10.4248/BR201304005

- [27] J. Vimort , M. McCormick , F. Budin , B. Paniagua. “Computing Textural Feature Maps for N-Dimensional images.” The Insight Journal (2017)
- [28] Q. Cao, A. Sisniega, J. W. Stayman, J. Yorkston, J. H. Siewerdsen, and W. Zbijewski (2019). Quantitative Cone-Beam CT of Bone Mineral Density Using Model-Based Reconstruction. Proceedings of SPIE--the International Society for Optical Engineering, 10948, 109480Y. <https://doi.org/10.1117/12.2513216>
- [29] I. A. Elbakri and J. A. Fessler, "Statistical image reconstruction for polyenergetic X-ray computed tomography," in IEEE Transactions on Medical Imaging, vol. 21, no. 2, pp. 89-99, Feb. 2002, doi: 10.1109/42.993128.
- [30] D.E. Whittier, S.K. Boyd, A.J. Burghardt, J. Paccou, A. Ghasem-Zadeaz, R. Chapurlat, K. Engelke, and M.L. Bouxsein. “Guidelines for the assessment of bone density and microarchitecture in vivo using high-resolution peripheral quantitative computed tomography.” Osteoporos Int. 2020 Sep;31(9):1607-1627. doi: 10.1007/s00198-020-05438-5.
- [31] L.J. Oostveen, K.L. Boedeker, M. Brink, M. Prokop, F. de Lange, and I. Sechopoulos. “Physical evaluation of an ultra-high-resolution CT scanner.” Eur Radiol. 2020 May;30(5):2552-2560. doi: 10.1007/s00330-019-06635-5.



# Curriculum Vitae

Gengxin Shi

## EDUCATION:

**Johns Hopkins University**, Baltimore, MD Sep 2018 - Present  
MSE, Biomedical Engineering with Imaging and Devices focus **GPA: 3.81/4.00**  
**The University of Iowa**, Iowa City, IA Sep 2013 - May 2018  
B.S, Biomedical Engineering with Bio-imaging focus (With Highest Distinction) **GPA:**  
**4.06/4.33**

## Honors:

- Dean's List: Fall 2013, Spring 2014, Spring 2015, Fall 2015, Fall 2016, Fall 2017, Spring 2018
- President's List: Fall 2015, Spring 2018

## PUBLICATIONS AND PRESENTATIONS:

- **G. Shi**, S. Sbramanian, Q. Cao, S. Demehri, J. H. Siewerdsen, and W. Zbijewski. "Application of a Novel Ultra-High-Resolution Multi-detector CT in Quantitative Imaging of Trabecular Microstructure." Proceedings of SPIE Medical Imaging 2020: Biomedical Applications in Molecular, Structural, and Functional Imaging (2020); 113171E (2020) <https://doi.org/10.1117/12.2552385>
- S.R. Miller, B. Singh, M. S. J. Marshall, C. Brown, N. Sheth, **G. Shi**, J. H. Siewerdsen, W. Zbijewski, and V. V. Nagarkar. "Pixelated Columnar CsI:Tl Scintillator for High Resolution Radiography and Cone-beam CT." Proceedings of SPIE Medical Imaging 2020: Physics of Medical Imaging (2020); 1131212 (2020) <https://doi.org/10.1117/12.2550196>
- **G. Shi**, S. Subramanian, Q. Cao, J. H. Siewerdsen, and W. Zbijewski. "Performance assessment of novel ultra-high-resolution multi-detector CT in quantitative imaging of trabecular microstructure." APS April meeting (2020)
- S. Subramanian, **G. Shi**, Q. Cao, M. Brehler, K. Shultz, J. W. Haller, S. Demehri, J. H. Siewerdsen, W. Zbijewski. "Quantitative evaluation of bone microstructure on a novel ultra-high-resolution whole-body CT." 105th Scientific Assembly and Annual Meeting of the Radiological Society of North America (2019)

## RESEARCH EXPERIENCE:

**Graduate Research Assistant**, Johns Hopkins University, Baltimore MD Sep 2018 – Present  
Imaging for Surgery, Therapy and Radiology Lab | Dr. Wojciech Zbijewski

- Performance assessment of new high resolution imaging technologies in quantitative assessment of trabecular bone microstructure:
  - Investigated accuracy and reproducibility of geometric and textural metrics of bone microstructure using three novel CT-based modalities:
    - Ultra-High Resolution CT
    - CMOS-based extremity Cone Beam CT (CBCT)

- Test-bench prototype CBCT with a recently developed pixelated scintillator
- Skills and experience:
  - Quantitative image biomarkers with application to bone imaging (texture, structure, composition)
  - Filtered back projection and model-based iterative reconstruction in CBCT
  - Image registration and transformation using MATLAB, MITK, Elastix, and Transformix
  - Advanced algorithms for trabecular bone segmentation
  - Phantom design for CT performance assessment
  - Dual Energy CT

**Graduate Level Course Project, Johns Hopkins University, Baltimore MD**

X-Ray Imaging and Computed Tomography | Dr. Wojciech Zbijewski Mar 2019 – May 2019

- CT Imaging performance assessment (image quality metrics, dose, artifacts).
- Implemented filtered back projection and model based iterative reconstruction (team project).

Imaging Instrumentation | Dr. J. Webster Stayman Mar 2019 – May 2019

- Programmed optical flow algorithm for object detection
- Improved image acquisition for better optical flow detection

Introduction to Data Science for Biomedical Engineering | Dr. Brian Caffo Mar 2019 – May 2019

- Prototyped a [Dual-Energy decomposition web-app](#) using Shiny (R)
- Utilized neural network using Keras (R) for image classification

Computer integrated surgery | Dr. Russell H. Taylor Sep 2018 – Dec 2018

- Implementation:
  - software package to perform calibration, simple registration, and tracking for a stereotactic navigation system
  - software to perform iterative registration to find the best transformation matching a given 3D surface to the reference
  - software to work with optical tracker where the 3D surface to be matched can be sampled using optical tracker tool tip
- Developed a Cartesian math package for 3D points with features including rotation and frame transformation and 3D to 3D point set registration

Surgery for Engineers | Dr. Jeffrey Siewerdsen Sep 2018 – Dec 2018

- Utilized 3D-Slicer in conjunction with optical tracking system to register a human lumbar spine phantom to a 3D model.
- Performed registration between 3D lumbar spine computer model, and CT and MRI human lumbar spine scans

Principles of Design of BME Instrumentation | Nitish V. Thakor Sep 2018 – Dec 2018

- Generated a working gaming controller prototype that enable quadriplegic to play racing games
- Prototyped home therapy for patients with complex regional pain syndrome (team project)
- Designed and Implemented the circuit and the control algorithm on Arduino

**Under-graduate Level Course Project, University of Iowa, Iowa City, IA**

Computers in Engineering | Dr. Mathews Jacob

Mar 2017 – May 2017

- Engineered an autonomous robot (3-Pi Robot) to follow a line-marked route and modulate speed based on road signs.
- Programmed the palolo 3Pi-Robot in C in collaboration

Software Design | Dr. Hans Johnson

Nov 2017 – Dec 2017

- Programmed an online messaging software in Java in collaboration

**SKILL and COMPETANCIES:**

**Computer skills**

- **Software** – MATLAB, ImageJ, MITK, 3D Slicer, Elastix, Keras, Shiny,
- **Programming** – C++, R, JAVA, and Arduino

**General skills**

- **Image registration, Signal Processing, Data Structures, Circuit Design, Neural Network, Machine Learning**
- **Organic Chemistry Procedures** – Extraction, Purification, NMR spectroscopy, Thin-layer Chromatography, Fractional Distillation, Templated reaction
- **Language** – Fluent in both English and Chinese